Role of Cerebellar GABAergic Dysfunctions in the Origins of Essential Tremor

Xu Zhang[1,2,3] and Sabato Santaniello[1,2,3*]

[1] Biomedical Engineering Department, University of Connecticut

[2] CT Institute for the Brain and Cognitive Sciences, University of Connecticut

[3] Brain Imaging Research Center, University of Connecticut

[*] **Correspondence:**

Sabato Santaniello

260 Glenbrook Road, Unit 3247
University of Connecticut
Storrs, CT 06269-3247 (USA)
Tel.: +1 (860) 486-4701
Email: sabato.santaniello@uconn.edu

SUMMARY

Essential tremor (ET) is among the most prevalent movement disorders but its origins are elusive. The inferior olivary nucleus (ION) has been hypothesized as the prime generator of tremor because of the pacemaker properties of ION neurons, but structural and functional changes in ION are unlikely under ET. Abnormalities have instead been reported in the cerebello-thalamo-cortical network, including dysfunctions of the GABAergic projections from the cerebellar cortex to the dentate nucleus. It remains unclear, though, how tremor would relate to a dysfunction of cerebellar connectivity. To address this question, we built a computational model of the cortico-cerebello-thalamo-cortical loop. We simulated the effects of a progressive loss of $GABA_A$ α_1-receptor subunits and upregulation of $\alpha_{2/3}$-receptor subunits in the dentate nucleus and, correspondingly, we studied the evolution of the firing patterns along the loop. The model closely reproduced experimental evidence for each structure in the loop. It showed that an alteration of amplitudes and decay times of the GABAergic currents to the dentate nucleus can facilitate sustained oscillatory activity at tremor frequency throughout the network as well as a robust bursting activity in the thalamus, which is consistent with observations of thalamic tremor cells in ET patients. Tremor-related oscillations initiated in small neural populations and spread to a larger network as the synaptic dysfunction increased, while thalamic high-frequency stimulation suppressed tremor-related activity in thalamus but increased the oscillation frequency in the olivocerebellar loop. These results suggest a mechanism for tremor generation under cerebellar dysfunction, which may explain the origin of ET.

KEYWORDS:

Essential Tremor, Purkinje Cells, Dentate Nucleus, Inferior Olivary Nucleus, GABA.

SIGNIFICANCE

We investigated the mechanisms of tremor generation in essential tremor (ET). Using computational modeling we show that tremor-related activity can originate from the olivocerebellar loop in response to a dysfunction and compensatory upregulation of GABA receptors in the dentate nucleus of cerebellum. The emerging tremor-related activity then projects to thalamus and reaches the cortico-thalamic motor loop. Consistent with clinical observations, the study shows that the tremor frequency decreases as the upregulation becomes stronger and increases as high-frequency stimulation is delivered to the thalamus. Our results provide an explanation of how local synaptic abnormalities would lead to widespread tremor-related neural activity in ET and suggests that compensatory processes in degenerative diseases may underlie brain dysfunction.

\body

1. INTRODUCTION

Essential tremor (ET) is a progressive neurological disease and among the most prevalent movement disorders (1). ET is characterized by a 4-12-Hz kinetic tremor that occurs in the upper limbs and may eventually spread to the neck and jaws, or accompany gait symptoms (2, 3). Clinically, only ~50% of the ET patients receive benefits from medications, while for the rest of the population deep brain stimulation (DBS) of the ventral intermediate thalamus (Vim) is the main alternative therapy (4). Despite large interest, the origins of ET remain unclear. It has been hypothesized that tremor has a central origin in the brainstem (5), where pacemaker neurons with prominent subthreshold oscillations in the range of ET frequencies have been identified in the inferior olivary nucleus (ION) (6, 7). Further evidence in support of this hypothesis has been provided by animal studies involving the injection of the neurotoxin harmaline (8, 9), which primarily targets ION neurons and causes generalized kinetic tremor. However, no consistent structural or functional change has been observed in the ION of ET patients compared with healthy controls (10-12). Evidence suggests, instead, that ET is associated with microstructural changes and neuronal dysfunctions in the cerebellum (13-15) including a loss of dendritic spines in Purkinje cells in the cerebellar cortex, a decrease in $GABA_A$ and $GABA_B$ receptors in the dentate nucleus, and a deficit of bound GABA transmitters (16-19). These changes have been correlated with the tremor severity (13) and may lead to significant alterations in the motor network (20, 21). It remains unclear, though, how these changes may relate to tremor.

Studies involving genetically modified mice (22, 23) have shown that the deletion of $GABA_A$ receptor α_1 subunits results in the loss of 50% of all $GABA_A$ receptors in the cerebellar structures and that such deletion is associated with kinetic tremor and motor incoordination, which are both

characteristics of ET. Furthermore, it has been reported that the loss of α_1 subunits is partially compensated by an overexpression of α_2 and α_3 subunits (23, 24), which colocalize with the α_1 subunits in the cerebellar nuclei and the molecular layer of the cerebellar cortex in rodents as well as humans (25, 26), and are responsible for longer opening of ion channels and slowly-decaying synaptic currents (27-29). Finally, an increase of tonic $GABA_A$ receptor-mediated currents has been reported in case of loss of α_1 subunits (30). Altogether, these studies indicate that a substantial modulation of the temporal dynamics of the GABAergic currents may occur in the cerebellum under ET condition.

Here, we constructed a computational model of the cortico-cerebello-thalamo-cortical (CCTC) loop and investigated whether changes to the dynamics of the GABAergic currents to the dentate nucleus may elicit tremor-related neuronal activity along the CCTC loop. The model includes single-compartment neurons from the brainstem (ION), the cerebellum (dentate nucleus and cerebellar cortex), the Vim, and the motor cortex (MC) according to a network topology derived from the primates' anatomy. The model reproduces the average firing rates and discharge patterns of single units in non-human primates and mice under normal conditions as well as tremor conditions for all modeled structures, where the recordings under tremor conditions were derived from animal studies involving the neurotoxin harmaline.

We show through numerical simulations that a progressive combination of reduced synaptic conductance and prolonged decay of the GABAergic currents in the synapses between Purkinje cells and deep cerebellar neurons may facilitate sustained oscillatory activity at the frequency of tremor in the olivocerebellar loop, i.e., ION, cerebellar cortex, and dentate nucleus. The oscillations propagate to the thalamocortical system (Vim-MC) and induce a sustained bursting activity in the Vim with characteristics that are consistent with the activity of tremor cells in ET patients

(31, 32). Consistent with clinical observations (33, 34), the frequency of the oscillatory activity slowly decreases by approximately 1 Hz as the manipulation of GABAergic currents progresses and is instead increased by about 0.4 Hz when electrical stimulation at the frequency of therapeutic DBS (185 Hz) is applied to Vim. DBS also reduces the range of GABAergic settings that can sustain tremor-related oscillations, thus suggesting that, even though primarily targeting the thalamocortical system, thalamic DBS may exert secondary effects on the olivocerebellar loop in ET patients. Finally, we show that neural oscillations leading to tremor-related bursting activity in the Vim can originate from a localized perturbation applied to a small portion of olivary neurons and spread through the entire cortico-olivo-cerebellar network, which further indicates the robustness of tremor-related neural dynamics and supports a possible network origin for ET.

2. RESULTS

The CCTC network model (Fig. 1A) includes: *(i)* the olivocerebellar loop, including 8 ION neurons in the brainstem (SI Appendix, *Fig. S1*A-D), 40 Purkinje cells (PC) and 4 granular layer clusters (GrL) in the cerebellar cortex (each GrL cluster includes 1 granule cell, 1 Golgi cell, and 1 stellate cell), and 1 glutamatergic deep cerebellar projection neuron (DCN) and 1 nucleo-olivary neuron (NO) in the dentate nucleus (SI Appendix, *Fig. S1*E-H); *(ii)* the thalamocortical system, including the Vim (1 thalamocortical neuron [TC]) and the MC (20 pyramidal neurons [PYN] and 2 fast-spiking interneurons [FSI]), see SI Appendix, *Table S1*. The connections between different neuron types are modeled using conductance-based synapses (SI Appendix, *Table S2*) and were constrained to reproduce the neuronal activity observed *in vivo* in PCs and DCN from healthy non-human primates during voluntary arm movements, see SI Appendix, *Fig. S2* (35). The connection graphs are reported in SI Appendix, *Fig. S3* and were determined to be consistent with the neuronal

anatomy in humans and animal models, as these structures are largely conserved across species (36). The relay function of the red nucleus (RN) along the dentato-rubro-olivary pathway (37-39) and of the pontine nuclei (PN) along the cortico-ponto-cerebellar pathway (40, 41), as well as the interneuron network (IN) in the cerebellar cortex (gray circles in Fig. 1A) are not explicitly modeled and are subsumed in the latency between pre- and postsynaptic structures, see SI Appendix, *SI Note 1*.

2.1. Model validation under normal and harmaline conditions.

In addition to reproducing the neuronal activity observed *in vivo* in Purkinje cells and deep cerebellar neurons from healthy non-human primates (SI Appendix, *Fig. S2*), the injected current parameters and synaptic gains in the CCTC loop were constrained such that the average firing rate of NO, TC, and PYN cells match the range of experimental values reported in (31, 37, 42) from *in vivo* recordings in healthy animals (NO: 5.5±2.0 Hz; TC: 26.6±4.2 Hz; PYN: 23.1±5.0 Hz, mean ± S.D.; values estimated over 60,000-ms-long simulation).

Fig. 1B-E shows the effects of the activation of ION neurons on the major projecting neurons in the cerebellum, i.e., PC and DCN, via climbing fibers. In response to ION activation, the PC exhibits a complex of spikes with amplitude and frequency modulation (*inset* in Fig. 1B), where the shape and duration of spikes matched experimental recordings from rodents (43), Fig. 1B-C. The PC then presents a long pause after the complex spike, which is consistent with data reported in ref. (44). The PC complex spiking contributes to the hyperpolarization of the DCN in the dentate nucleus and the consequent formation of rebound bursts, which are consistent with data in refs. (45, 46), Fig. 1D-E.

When simulated under normal condition, the TC neuron in the Vim spikes irregularly (Fig. 2G) as reported in ref. (31) while the ION neurons exhibit subthreshold oscillations at 5.6 Hz, which

are well-aligned with *in vivo* recordings from rodents (47, 48). The rare occurrence of spikes in the ION neurons (Fig. 2A) reflects the fact that ION neurons mainly respond to sensory stimuli, while their probability of spiking becomes minimal during movements (49, 50).

To verify that the CCTC model is able to reproduce the experimental tremor conditions induced by harmaline, we simulated the localized effects of the neurotoxin harmaline on the ION neurons by potentiating the calcium channels as in ref. (6), see *MATERIALS AND METHODS*. The direct effect of this change is a spontaneous synchronous firing of the ION neurons at 7.1 Hz ("tremor frequency"), consistent with the frequency of harmaline tremor in the primate model (51). We tracked the effects of the ION synchronous firing on the network and we confirmed a periodic bursting pattern in the Vim (burst duration: 102.1±15.0 ms, mean burst frequency: 7.1 Hz across three instances of the CCTC model), Fig. 2H. Accordingly, the power spectral density of the Vim showed a strong peak at the tremor frequency and followed the spectrum of tremor cells recorded in ET patients *in vivo* (31), Fig. 2I-J.

The mechanism of propagation of the oscillations from the ION to the Vim depends on a significant shift in the discharge pattern of the PCs and the DCN associated with these oscillations: the PCs shift from tonic firing with occasional complex spikes and pauses (Fig. 2C) to periodic complex spikes (Fig. 2D) driven by the sustained ION activation (Fig. 2B) through the climbing fibers, while the DCN transitions from irregular firing to sequences of rebound bursts at the tremor frequency (burst duration: 109.4±9.7 ms; inter-burst intervals: 30.3±4.6 ms; mean ± S.D.), see Fig. 2E-F. Overall, these results indicate that the olivocerebellar (ION→PC→DCN) pathway can facilitate the propagation of oscillations within the tremor frequency band (4-12 Hz) towards the thalamocortical system.

2.2. GABAergic dysfunction in the DCN facilitates olivocerebellar oscillations.

To explore the relationship between cerebellar GABAergic dysfunctions and the possible origins of ET, we simulated the concurrent loss of $GABA_A$ α_1-receptor subunits and upregulation of α_2/α_3-receptor subunits in the cerebellum by progressively lowering the maximum synaptic conductance $g_{PC\rightarrow DCN}$ and increasing the decay time $\tau^{PC\rightarrow DCN}$ of the synaptic currents from PCs to DCN (range: 2-24 ms; nominal value under normal conditions: 2.4 ms, see SI Appendix, *SI Note 1* and *Table S2*). The effect of these changes was a progressive modulation of the shape and duration of the synaptic currents, which span the range reported *in vitro* (28, 30, 52) that goes from the normal composition of α_1-receptor subunits to the complete dominance of α_2/α_3-receptor subunits. The GABAergic currents to NO, instead, were not altered because they are significantly smaller than the currents to DCN (53) and mainly mediated by α_3-receptor subunits (54), which make these currents more than 10-fold slower than the currents to DCN (see $\tau^{PC\rightarrow NO}$ in SI Appendix, *Table S2*) and less likely to be affected by ET.

Fig. 3A reports the range of values tested for $\tau^{PC\rightarrow DCN}$ and the ratio $\mathcal{R}$ between the synaptic gains $g_{PC\rightarrow DCN}$ and $g^*_{PC\rightarrow DCN}$, where $g^*_{PC\rightarrow DCN}$ is the nominal conductance value under normal conditions. An initial perturbation consisting of a single 20-ms-long depolarizing current pulse (10 pA) was delivered at time t=1,000 ms to the ION neurons to mimic a transient exogenous stimulus from afferent projections (SI Appendix, *Fig. S4*). The spiking activity of the ION neurons and the Vim PSD were monitored in the following 3,000 ms. The region with tremor was defined as the parameter combinations ($\mathcal{R}$, $\tau^{PC\rightarrow DCN}$) for which any ION neuron sustained spiking for >2,000 ms after an initial perturbation. Correspondingly, the power spectrum of the Vim was inspected and the peak frequency (i.e., the frequency of peak PSD value) was used as a proxy of the tremor activity if within the band 4-12 Hz.

As reported in Fig. 3A, the range of ratios $\mathcal{R}$ that can sustain tremor activity increases with

longer $\tau^{PC\rightarrow DCN}$. Moreover, as the pair ($\mathcal{R}$, $\tau^{PC\rightarrow DCN}$) moves towards the lower right quadrant of Fig. 3A (i.e., further degeneration of the GABAergic currents), the frequency of tremor decreases by approximately 1 Hz, thus showing a progressive adjustment that matches longitudinal observations reported in ET patients (33, 34). We also assessed the role of the NO in forming tremor-related network oscillations. Specifically, we repeated the simulations in Fig. 3A with the synaptic strength of the NO→ION projection decreased by 50%. The results are reported in SI Appendix, *Fig. S5* and indicate that the tremor region is enlarged when the NO neuron exerts less inhibitory input into the ION neurons, which suggests that the NO neurons may regulate the susceptibility of the network to enter into tremor-related oscillations.

As in the harmaline condition, the cerebellar GABAergic dysfunctions (denoted here as "ET condition") were associated with a tonic synchronous spiking of the ION neurons, which led to the Vim activity in the tremor band 4-12 Hz. Differently from the harmaline condition, though, a significant change of the bursting pattern was observed in the discharge pattern of the DCN. Fig. 3B-E report the burst analyses for the DCN under harmaline and one ET condition (yellow circle in Fig. 3A). Although in both cases the ION neurons spiked synchronously and DCN exhibited similar bursting frequencies (Fig. 3B), the DCN fired shorter bursts with higher intra-burst rates and longer inter-burst intervals (Fig. 3C-E) under ET condition, which reflect a prolonged periodic presynaptic inhibition (see SI Appendix, *Fig. S4* for the behavior of other structures). Note that the ET condition was obtained with no manipulation of the properties of the ION neurons. This indicates that a manipulation of the bidirectional interaction between the ION and the cerebellar structures, which is secondary to the cerebellar GABAergic dysfunctions, can enable and facilitate widespread network oscillations that would ultimately lead to the tremulous activity in the Vim.

2.3. Phase-dependent excitation of ION neurons underlies persistent network oscillations

To determine the mechanism of tremor generation in ET, we focused on the di-synaptic excitatory pathway from DCN to ION neurons, i.e., the dentato-rubro-olivary projection. Since it has been indicated that ION neurons spike in response to exogenous depolarizing stimuli at a preferred phase of the subthreshold membrane voltage oscillation (48), we isolated the ION model and controlled the timing of the input to the ION neurons by delivering a suprathreshold depolarizing current pulse to all ION neurons at a specific onset time T after the last ION spike. We varied both the amplitude of the pulse (I_{STEP}, range: 0-1.0 pA, which is comparable to the range of synaptic input from DCN) and T (up to 175 ms, which is approximately the subthreshold oscillation period of ION). The pulse was kept ON till any of the 8 ION neurons fired an action potential (Fig. 4A, red curve), in which case the stimulus was then turned OFF and reapplied with the same onset T after the new ION neuron's spike. Accordingly, the ION neurons received a train of current pulses with the same amplitude and time-varying durations, all delivered at approximately the same phase of their subthreshold oscillation. If the current pulse did not trigger another spike from any ION neuron until the end of the subthreshold oscillation cycle (Fig. 4A, black curve), then that specific parameter pair (I_{STEP}, T) would be labeled as unable to trigger ION spiking. Fig. 4B shows that stimuli delivered at earlier phases of the subthreshold oscillation, e.g. T<50 ms, would hardly trigger ION spiking and would therefore prevent the olivocerebellar system to engage in tremor-related oscillations (Fig. 4B, gray background). Stimuli delivered at a later onset, instead, robustly sustained ION spiking and the frequency of the spikes depends on both the pulse intensity I_{STEP} and the specific onset T. Furthermore, as shown in Fig. 4C, the average ION firing rate increases with the pulse intensity I_{STEP} but the relationship between the pulse duration, which is related to the pulse onset, and the firing rate is nonlinear, with the highest ION firing rate occurring for pulse durations in the range 60-80 ms. This indicates that the ION neurons are highly selective against

the timing of the input excitation and that the ION spiking is most efficiently triggered by inputs arriving at a specific timing.

Finally, for each pair ($\mathcal{R}$, $\tau^{PC\rightarrow DCN}$), we compared the predictions of the isolated ION model in Fig. 4B to the net synaptic input delivered from DCN to ION neurons via RN in the full CCTC model. We measured the average lag between the onset of each DCN burst and the onset of the ION action potential that precedes it (i.e., $\Delta_{ION\rightarrow DCN\_burst}$ in Fig. 4D). As shown in Fig. 4E, 91.8% of the pairs (904 out of 985) that resulted in tremor at the Vim, had $\Delta_{ION\rightarrow DCN\_burst}$>50 ms, which is consistent with the map in Fig. 4B for sustained ION spiking. Similarly, in 85.4% of the pairs (696 out of 815) in the tremor-free region (white area in Fig. 3A), the average $\Delta_{ION\rightarrow DCN\_burst}$ was below 50 ms. Altogether, these results indicate that the changes in the shape of the GABAergic currents may facilitate the generation of sustained spiking in the ION neurons at tremor frequencies by modulating the duration and rate of the bursting activity of DCN, which activated the ION neurons robustly through the dentato-rubro-olivary pathway (RN pathway in Fig. 4D, panel a).

To further elucidate the tremor generation mechanism, Fig. 4D reports the timing of action potentials in ION, PC, and DCN neurons under normal (panels b,d,f) and ET conditions (panels c,e,g). Under normal conditions, the short inter-burst interval of the DCN is inefficient in activating the ION. In presence of GABAergic dysfunctions to the PC-DCN connection, instead, the olivary activation can cause a prolonged hyperpolarization of the DCN, which is followed by a rebound burst that is in resonance with the ION subthreshold oscillatory activity. The glutamatergic post-synaptic currents elicited by the DCN activity via the RN pathway (Fig. 4D panel b-c) can therefore effectively trigger recurrent ION spikes.

2.4. Therapeutic Vim DBS enhances the frequency of network oscillations.

High-frequency (150-185 Hz) DBS of the Vim is clinically recognized for the treatment of

essential tremor (55). Although effective at reducing the amplitude of the tremor, Vim DBS is known to alter secondary pathophysiologic characteristics of ET, including tremor frequency and regularity, without restoring these characteristics to normal conditions (34, 56). Accordingly, we investigated the effects of Vim DBS at 185 Hz on the oscillatory activity in the olivocerebellar loop for every pair ($\mathcal{R}$, $\tau^{PC\rightarrow DCN}$) considered in Fig. 3A. DBS was simulated as a train of square current pulses (pulse width: 0.2 ms) whose amplitude (10 nA) was chosen to be subthreshold to elicit tonic firing activity in the Vim (average rate: 92.6±0.5 Hz, mean ± S.D.) and to suppress the tremor peak in the Vim power spectral density as in (57) for all pairs ($\mathcal{R}$, $\tau^{PC\rightarrow DCN}$), see Fig. 5A.

Despite suppressing the bursting activity in the Vim, the ION and DCN neurons continued to spike and burst, respectively, at the tremor frequency. The range of pairs ($\mathcal{R}$, $\tau^{PC\rightarrow DCN}$) that resulted in sustained activity, though, was reduced by 18.8% when compared to the case without DBS while the spiking frequency of the ION neurons across all pairs ($\mathcal{R}$, $\tau^{PC\rightarrow DCN}$) in the tremor region increased by 4.2±3.9% (mean ± S.D.), Fig. 5B. Furthermore, we analyzed the burstiness of the DCN for the pair of parameters ($\mathcal{R}$, $\tau^{PC\rightarrow DCN}$) considered in Fig. 3B-E (ET case) and we found that, when 185-Hz-Vim-DBS was applied, the length of the DCN inter-burst intervals decreased by 21.3±14.8% (mean ± S.D.). Finally, we quantified the effects of the Vim DBS frequency on the olivocerebellar system by measuring the burstiness of the DCN patterns and the average ION firing rate as the DBS frequency varied from 2.5 Hz to 185 Hz. We found that the average DCN inter-burst interval duration decreased as the DBS frequency increased (Fig. 5C) and the regularity of the DCN bursts increased (i.e., decreased coefficient of variation of the inter-burst durations, *inset* to Fig. 5C), while the average ION firing rate increased (Fig. 5D). Furthermore, both changes in ION and DCN activity became more stable for DBS frequencies above 100 Hz (plateau effect, see Fig. 5C-D).

Since no antidromic effect of DBS onto the cerebellothalamic pathway was included in our model, we hypothesized that the changes to the dentate nucleus and ION neurons were mediated by a modulation of the cortico-ponto-cerebellar pathway. *Fig. S6*A in SI Appendix reports the average firing rate of the pyramidal neurons (PYN) as the DBS frequency increased from 0 Hz (i.e., no DBS) to 185 Hz and it shows that the PYN firing rate grew linearly as the DBS frequency increased from 0 Hz to 100 Hz and then plateaued at the DBS frequency range 100-185 Hz. The increase in the PYN firing rate was inversely correlated with the average DCN inter-burst interval duration (SI Appendix, *Fig. S6*B) and positively correlated with the average ION spiking rate (SI Appendix, *Fig. S6*C), respectively.

Altogether, these results indicate that, while effective at masking the tremor activity in the thalamocortical system, Vim DBS does not eliminate tremor-related oscillatory activity in the olivocerebellar system. The DBS-mediated increment in cortical excitability, however, may counteract the prolonged hyperpolarization of the deep cerebellar neurons and therefore modulate the oscillations in the olivocerebellar system. These modulatory effects may explain the increased tremor frequency but reduced tremor intensity in ET patients under therapeutic Vim DBS (34).

2.5. Tremor oscillations could spread across multiple olivocerebellar loops.

To further assess the robustness of the tremor-related oscillations emerging in the olivocerebellar system under GABAergic dysfunction as the size and complexity of the CCTC loop increases, we expanded the original CCTC network by scaling up the number of neurons included in the model by a factor 5. The resultant scale-up CCTC model included 425 single-compartment neurons with similar ratios between neural populations. In addition, the interconnections between neurons in each population as well as the di-synaptic projections between DCN and ION neurons were randomized to avoid the formation of local closed-loop circuits between neurons in the cerebellum

and ION. See SI Appendix, *SI Note 3* for details.

Under normal condition, an initial perturbation as described in section 2.2 above was applied to all ION neurons (40 out of 40) simultaneously but no ION neuron eventually engaged into tonic spiking activity, which led to no sustained oscillations throughout the network (Fig. 6A, C, E) and no tremor frequency in the Vim spectrogram (Fig. 6G). Vice versa, under ET condition, we varied the number of ION neurons that received the initial perturbation and we determined whether sustained oscillations throughout the network were elicited. The ION neurons receiving the perturbation were chosen among those interconnected by gap junctions. Across five instances of the scale-up model, we found that an initial perturbation delivered to approximately 50% of the ION neurons (average: 20.8±5.4, mean ± S.D.; min: 16; max: 30) elicited a sustained spiking activity in the entire ION population within 500 ms (e.g., see example in Fig. 6B), along with complex spikes in the PCs and sustained bursting activity in the DCNs (Fig. 6D, F). The resultant widespread network oscillation was then associated with a sustained tremor activity in the Vim (Fig. 6H).

Overall, the spread of tremor-related oscillations across multiple olivocerebellar loops indicates that, under GABAergic dysfunction, the olivocerebellar system is highly susceptible to perturbations and can rapidly converge to global, tremor-related oscillatory dynamics.

3. DISCUSSION

The cellular origins of ET have been intensively investigated over the past twenty years. The presence of tremor cells in the cerebellum-recipient regions of thalamus in ET patients (31) indicates that the cerebellothalamic pathway is pivotal to the generation of tremor. Moreover, ref. (58) reported an abnormal eyeblink conditioning in patients with ET, which suggests that the olivocerebellar system may be functionally impaired. Furthermore, studies (16, 59, 60) have reported

several microstructural alterations in the cerebellar cortex of ET patients, including a diffused loss of the Purkinje cells, reduced dendritic arborizations, and axonal swellings, which may severely alter the cerebellar activity. Studies (17-19) have also reported a significant increment of $GABA_A$ receptor binding sites in the cerebellum and, locally, a significant decrease of $GABA_A$ and $GABA_B$ receptors in the dentate nucleus in ET patients. Finally, disorders that involve cerebellar dysfunction like motor learning impairment, are frequently reported in ET subjects (61) along with a generalized hyperactivation of the cerebellar structures during movements (13, 62). Altogether, these results have contributed to the hypothesis that a cerebellar dysfunction may lead to pathologic activity along the cerebellothalamic pathway. It is unclear, though, how tremor-related activity in the Vim could result from such a variety of changes reported in the cerebellum. Our model provides a mechanistic explanation that reconciles several, apparently contradicting experimental observations. The following predictions are made.

Tremor oscillations may have network origins. Studies (15, 20, 21, 63) have reported diffused alterations to the functional networks among cerebellum, thalamus, and cortices during motor tasks in ET subjects, including a significant reduction of the connectivity between cortical and cerebellar motor areas as well as between cerebellar cortex and dentate nuclei, and an increment in low-frequency oscillatory activity in the motor cortices. Both the reduction in connectivity and the increment in low-frequency oscillations positively correlated with the severity of kinetic tremor, thus suggesting a link between network dysfunctions and tremor. Although it is unclear how oscillations in the cerebellum affect the activity of the cerebral cortex, it has been suggested that the structural alterations in the cerebellum may alter the cerebellar output to the cortico-thalamo-cerebellar networks, thus contributing to the disruption of the connectivity in these functional networks (20).

Our study identifies a potential network-based mechanism to sustain and amplify tremor-related neural oscillations. We predict that such oscillations are sustained by the interplay between inferior olivary nucleus, dentate nucleus, and cerebellar cortex. The oscillatory activity propagates along the olivocerebellar pathway into the cerebellum and re-enters the olivary nucleus through the dentato-rubro-olivary pathway. In addition, localized perturbations to a small portion of neurons in the inferior olive nucleus can initiate neural oscillations that quickly spread to a larger network and eventually alter the thalamocortical discharge patterns. This prediction reconciles the role of the inferior olivary nucleus in maintaining neural oscillations with the lack of olivary dysfunctions reported in ET patients (10-12) and suggests that the olivary neurons may be recruited into tremor oscillations via the dentato-rubro-olivary pathway because of their intrinsic pacemaker capabilities, with no need for specific alterations of the ion channels or synapses.

Although there is little knowledge about the dentato-rubro-olivary pathway, studies in ET patients have recently suggested that this pathway may be involved in tremor generation (64, 65). It is also known that drugs (e.g., alcohol) that interfere with the synaptic transmissions along this pathway can attenuate tremor symptoms and reduce the size of Purkinje cells' complex spikes following climbing fiber activation (66, 67). Our model predicts that the reduction in complex spikes would result in shorter hyperpolarization and weaker rebound firing of the deep cerebellar neurons, and therefore cause a decreased activity of the dentato-rubro-olivary pathway, which is consistent with observations reported in ref. (66). We expect that the manipulation of this pathway in animal models, e.g., via optogenetic stimulation of the red nucleus, might help further assess the role in ET.

Slow-decaying GABAergic currents in the dentate nucleus contribute to sustained neural oscillations. It has been speculated that the loss of Purkinje cells and the structural changes to the

cerebellar cortex may cause a reorganization of the Purkinje cell functional network as well as the interface between climbing fibers and Purkinje cells (2). This reorganization would result in a reduced GABAergic modulation of the dentate nuclei and a facilitation of the pacemaker activity of the DCN cells, which would eventually propagate to the thalamus (2). Our study suggests that a nonspecific reduction in the GABAergic currents to the DCN can increase its average firing rate and thus the glutamatergic input to the thalamus, but it does not lead to a rhythmic activity in the tremor band either in the DCN or Vim. This is supported by the observation that deep cerebellar neurons rarely exhibit spontaneous pacemaker activity at frequencies within the tremor band (68). This is also consistent with earlier studies, e.g., (69), which reported that the degeneration of Purkinje cells alone may be insufficient to elicit sustained oscillations in the Vim, while highly synchronized afferent currents from the deep cerebellar structures are required to recruit the thalamocortical neurons.

Our study suggests that the temporal dynamics of the GABAergic currents may be critical for tremor generation. Although none of the parametric changes that we applied to the GABAergic currents were sufficient to initiate tremor-related network oscillations in our model, we found that a specific range of GABAergic currents to the dentate nucleus can make these oscillations outlast the initial perturbation and self-sustain. This suggests that the role of the cerebellar dysfunctions in ET may be related to the preservation, amplification, and propagation of the tremor oscillations. Moreover, the need for an initial perturbation may be linked to the fact that tremor oscillations in the thalamus are enabled by voluntary movement, while absent at rest (31).

On the other hand, the preservation of network oscillations depends on the dynamics of the GABAergic currents. Specifically, the GABAergic dysfunctions between Purkinje cells and dentate neurons may reduce the fast α_1-subunit-mediated currents and increase the slowly-decaying

currents mediated by the upregulated $\alpha_{2/3}$ subunits (23-26). Our model predicts that such currents can facilitate the after-hyperpolarization rebound of the deep cerebellar neurons, which robustly activates the olivary neurons at a preferred phase of their subthreshold oscillations, thus facilitating the synchronization along the olivocerebellar loop. Also, other ET-related pathologies such as the increased Purkinje cell axonal branching, recurrent collaterals, and terminal axonal sprouting, may further amplify such synchronization and therefore exacerbate tremor symptoms, even with substantial losses of inferior olive neurons and Purkinje cells (70, 71).

Finally, our model shows that the range of tremor-related GABAergic currents to the dentate nucleus increases as the synaptic current from the nucleo-olivary neurons to the inferior olivary nucleus (NO→ION) decreases. This is mediated by an increment of the connectivity between olivary neurons, which occurs because the modeled NO→ION pathway has an inhibitory effect on the gap junctions between olivary neurons. The net effect is consistent with the regulatory action of the NO→ION pathway on the neuronal coupling in the inferior olivary nucleus (72). However, the interaction between ION and NO neurons involves additional connections, such as the projections from climbing fibers to NO neurons (73), which are currently neglected in our model and may contribute a negative feedback to the ION neurons. In addition, the specific localization of the NO synapses on the ION neurons and the morphology of the dendrites of ION neurons may significantly steer the synchronization within the inferior olivary nucleus (72, 74-76). Accordingly, it is plausible that the NO-ION connectivity may affect the network oscillations. For instance, it is possible that the adaptation of the discharge pattern of NO and ION neurons may result in a wider range of oscillation frequencies across the entire network than in our model. Similarly, as the ION neurons form groups of densely coupled neurons interspersed with areas of weak coupling (75), it is possible that different circuits along the olivocerebellar pathway have oscillations at slightly

418 different frequencies, thus resulting in a more complex spreading of the neural oscillations through
419 the network.

420 ***Neurostimulation modulates tremor networks.*** Currently, Vim DBS remains the most suc-
421 cessful neurostimulation therapy for ET. We investigated the effects of Vim DBS on different
422 structures in the CCTC model. Although our representation of DBS aimed to mimic the shift in
423 discharge pattern in Vim (57) and therefore lacks explicit representation of other mechanisms (77),
424 the local effects of Vim DBS on the thalamocortical and pyramidal neurons were consistent with
425 recordings in ET subjects, showing a robust attenuation of the tremor oscillations in the Vim and
426 activation of the motor cortex (78). Our results show that, although the main effect of Vim DBS
427 likely involves blocking tremor oscillations at thalamocortical level (77), through an increment in
428 cortical excitability, it also has secondary effects on the neural oscillations in the olivocerebellar
429 structures, which received a shift in frequency consistent with clinical observations (34, 56). It also
430 provides an explanation for the higher tremor frequency in kinetic versus postural tasks, since the
431 former presumably involve a higher motor cortical activity (79). Altogether, these predictions sug-
432 gest that the oscillations underlying ET may involve a large network including both the cerebellar
433 and cerebral structures.

434

435 ## 4. MATERIALS AND METHODS

436 ### 4.1. Computational model.

437 We developed a network of 85 single-compartment model neurons (73 biophysically based
438 neurons and 12 leaky integrate-and-fire neurons). The equations and parameters for the model
439 neurons of PC, GrL cluster, TC, PYN, and FSI were obtained from refs. (80-83), respectively, and
440 modified as reported in SI Appendix, *SI Note 1*. The ION neuron included the soma compartment

of the multicompartment model in ref. (48) with calcium channel equations from refs. (84, 85), which account for the reduction to single-compartment and fit *in vitro* recordings from rodents reported in ref. (85). The DCN model neuron included the soma compartment of the multicompartment model in ref. (86), with ion channel conductance values adjusted to account for the reduction to single-compartment (see SI Appendix, *Table S1*). The NO model neuron was derived from the DCN model and includes fast sodium channels, fast and slow delayed rectifier potassium channels, and leaky channels with parameters adjusted to match the *in vitro* recordings in (54) as shown in SI Appendix, *Fig. S2*E-H (model described in SI Appendix, *SI Note 1*). The ratios of PCs to DCN (40:1) and PYNs to FSIs (20:2) were as in refs. (87) and (88), respectively, and account for the convergence of PCs onto DCNs, as well as the extensive connectivity of the cortical pyramidal neurons and interneurons. Details about the network connectivity are reported in SI Appendix, *SI Note 1* and *Fig. S3*.

Each neuron was endowed with a constant current (I_{OC}) to simulate the background excitation and a Gaussian noise with zero mean to simulate the subthreshold membrane voltage fluctuations (±5 mV). The intensity of current I_{OC} varied across the ION neurons (uniform distribution) to generate subthreshold oscillations at different frequencies. Similarly, the intensity of I_{OC} varied across the PCs (gamma distribution) to simulate a range of spontaneous firing rates. See values in SI Appendix, *Table S1* and *Table S2*. The transition from normal conditions to harmaline-induced tremor conditions was simulated by modifying the ION model neuron as proposed in ref. (48). Briefly, the maximum conductance of the ION calcium channels was increased from 0.27 to 0.3 $mS \cdot cm^2$ and the maximum conductance of h-type channels was lowered from 0.08 to 0.02 $mS \cdot cm^2$ to mimic the experimental conditions reported in ref. (6), while the intensity of I_{OC} was set to 2 pA for all ION neurons. Accordingly, all ION neurons presented subthreshold oscillations at the same

frequency and became spontaneously active, with one action potential fired by each neuron in synchrony per oscillation cycle.

4.2. Computational tools.

In each analysis, three different instances of the model network were generated. Numerical simulations were programmed in NEURON, ver. 7.5 (89) and run on an eight-core Intel Xeon workstation (3.6 GHz/core, 16 GB RAM). The differential equations were integrated via CVODE method with time step 0.0125 ms. Results were analyzed in MATLAB R2017a (The MathWorks, Inc.). We implemented published algorithms to compute firing and burst rates, power spectral densities, and cross-correlation as in refs. (90, 91). Further details about the implementation are given in SI Appendix, *SI Note 2*. The NEURON code implementing the proposed model will be made available on ModelDB (https://senselab.med.yale.edu/modeldb/).

5. ACKNOWLEDGEMENTS

This work was partly supported by the CT Institute for the Brain and Cognitive Sciences IB-RAiN Fellowship (to X.Z.) and the US National Science Foundation CAREER Award 1845348 (to S.S.).

REFERENCES

1. Louis ED & Ferreira JJ (2010) How common is the most common adult movement disorder? Update on the worldwide prevalence of essential tremor. *Mov Disord* 25(5):534-541.
2. Louis ED (2018) Essential tremor and the cerebellum. *Handb Clin Neurol* 155:245-258.
3. Bhatia KP, *et al.* (2018) Consensus Statement on the classification of tremors. from the task force on tremor of the International Parkinson and Movement Disorder Society. *Mov Disord* 33(1):75-87.
4. Lyons KE & Pahwa R (2004) Deep brain stimulation and essential tremor. *J Clin Neurophysiol* 21(1):2-5.
5. DeLong MR (1978) Possible involvement of central pacemakers in clinical disorders of movement. *Fed Proc* 37(8):2171-2175.
6. Park YG, *et al.* (2010) Ca(V)3.1 is a tremor rhythm pacemaker in the inferior olive. *Proc Natl Acad Sci U S A* 107(23):10731-10736.

7. Llinas R & Yarom Y (1981) Electrophysiology of mammalian inferior olivary neurones in vitro. Different types of voltage-dependent ionic conductances. *J Physiol* 315:549-567.

8. Lamarre Y & Mercier LA (1971) Neurophysiological studies of harmaline-induced tremor in the cat. *Can J Physiol Pharmacol* 49(12):1049-1058.

9. Llinas R & Volkind RA (1973) The olivo-cerebellar system: functional properties as revealed by harmaline-induced tremor. *Exp Brain Res* 18(1):69-87.

10. Louis ED, Babij R, Cortes E, Vonsattel JP, & Faust PL (2013) The inferior olivary nucleus: a postmortem study of essential tremor cases versus controls. *Mov Disord* 28(6):779-786.

11. Bucher SF, Seelos KC, Dodel RC, Reiser M, & Oertel WH (1997) Activation mapping in essential tremor with functional magnetic resonance imaging. *Ann Neurol* 41(1):32-40.

12. Hallett M & Dubinsky RM (1993) Glucose metabolism in the brain of patients with essential tremor. *J Neurol Sci* 114(1):45-48.

13. Pagan FL, Butman JA, Dambrosia JM, & Hallett M (2003) Evaluation of essential tremor with multi-voxel magnetic resonance spectroscopy. *Neurology* 60(8):1344-1347.

14. Wills AJ, Jenkins IH, Thompson PD, Findley LJ, & Brooks DJ (1995) A positron emission tomography study of cerebral activation associated with essential and writing tremor. *Arch Neurol* 52(3):299-305.

15. Yin W, Lin W, Li W, Qian S, & Mou X (2016) Resting State fMRI Demonstrates a Disturbance of the Cerebello-Cortical Circuit in Essential Tremor. *Brain Topogr* 29(3):412-418.

16. Louis ED*, et al.* (2014) Reduced Purkinje cell dendritic arborization and loss of dendritic spines in essential tremor. *Brain* 137(Pt 12):3142-3148.

17. Paris-Robidas S*, et al.* (2012) Defective dentate nucleus GABA receptors in essential tremor. *Brain* 135(Pt 1):105-116.

18. Boecker H*, et al.* (2010) GABAergic dysfunction in essential tremor: an 11C-flumazenil PET study. *J Nucl Med* 51(7):1030-1035.

19. Gironell A*, et al.* (2012) Gaba and serotonin molecular neuroimaging in essential tremor: a clinical correlation study. *Parkinsonism Relat Disord* 18(7):876-880.

20. Buijink AW*, et al.* (2015) Motor network disruption in essential tremor: a functional and effective connectivity study. *Brain* 138(Pt 10):2934-2947.

21. Gallea C*, et al.* (2015) Intrinsic signature of essential tremor in the cerebello-frontal network. *Brain* 138(Pt 10):2920-2933.

22. Kralic JE*, et al.* (2005) Genetic essential tremor in gamma-aminobutyric acidA receptor alpha1 subunit knockout mice. *J Clin Invest* 115(3):774-779.

23. Kralic JE, Korpi ER, O'Buckley TK, Homanics GE, & Morrow AL (2002) Molecular and pharmacological characterization of GABA(A) receptor alpha1 subunit knockout mice. *J Pharmacol Exp Ther* 302(3):1037-1045.

24. Fritschy JM & Panzanelli P (2006) Molecular and synaptic organization of GABAA receptors in the cerebellum: Effects of targeted subunit gene deletions. *Cerebellum* 5(4):275-285.

25. Stojanovic T*, et al.* (2016) The alpha1, alpha2, alpha3, and gamma2 subunits of GABAA receptors show characteristic spatial and temporal expression patterns in rhombencephalic structures during normal human brain development. *J Comp Neurol* 524(9):1805-1824.

26. Kralic JE*, et al.* (2006) Compensatory alteration of inhibitory synaptic circuits in cerebellum and thalamus of gamma-aminobutyric acid type A receptor alpha1 subunit knockout mice. *J Comp Neurol* 495(4):408-421.

27. Ortinski PI, Lu C, Takagaki K, Fu Z, & Vicini S (2004) Expression of distinct alpha subunits of GABAA receptor regulates inhibitory synaptic strength. *J Neurophysiol* 92(3):1718-1727.

28. Dixon C, Sah P, Lynch JW, & Keramidas A (2014) GABAA receptor alpha and gamma subunits shape synaptic

currents via different mechanisms. *J Biol Chem* 289(9):5399-5411.

29. Ramadan E*, et al.* (2003) GABA(A) receptor beta3 subunit deletion decreases alpha2/3 subunits and IPSC duration. *J Neurophysiol* 89(1):128-134.
30. Ortinski PI*, et al.* (2006) Deletion of the GABA(A) receptor alpha1 subunit increases tonic GABA(A) receptor current: a role for GABA uptake transporters. *J Neurosci* 26(36):9323-9331.
31. Hua SE & Lenz FA (2005) Posture-related oscillations in human cerebellar thalamus in essential tremor are enabled by voluntary motor circuits. *J Neurophysiol* 93(1):117-127.
32. Chen H*, et al.* (2010) Neuronal firing in the ventrolateral thalamus of patients with Parkinson's disease differs from that with essential tremor. *Chin Med J (Engl)* 123(6):695-701.
33. Elble RJ (2000) Essential tremor frequency decreases with time. *Neurology* 55(10):1547-1551.
34. Vaillancourt DE, Sturman MM, Verhagen Metman L, Bakay RA, & Corcos DM (2003) Deep brain stimulation of the VIM thalamic nucleus modifies several features of essential tremor. *Neurology* 61(7):919-925.
35. Thach WT (1968) Discharge of Purkinje and cerebellar nuclear neurons during rapidly alternating arm movements in the monkey. *J Neurophysiol* 31(5):785-797.
36. Ashida R, Cerminara NL, Brooks J, & Apps R (2018) Principles of organization of the human cerebellum: macro- and microanatomy. *Handb Clin Neurol* 154:45-58.
37. Bazzigaluppi P, Ruigrok T, Saisan P, De Zeeuw CI, & de Jeu M (2012) Properties of the nucleo-olivary pathway: an in vivo whole-cell patch clamp study. *PLoS One* 7(9):e46360.
38. Ruigrok TJ & Voogd J (1995) Cerebellar influence on olivary excitability in the cat. *Eur J Neurosci* 7(4):679-693.
39. Oka H & Jinnai K (1978) Electrophysiological study of parvocellular red nucleus neurons. *Brain Res* 149(1):239-246.
40. Sasaki K, Kawaguchi S, Shimono T, & Prelevic S (1970) Electrophysiological studies of the pontine nuclei. *Brain Res* 20(3):425-438.
41. Palesi F*, et al.* (2017) Contralateral cortico-ponto-cerebellar pathways reconstruction in humans in vivo: implications for reciprocal cerebro-cerebellar structural connectivity in motor and non-motor areas. *Sci Rep* 7(1):12841.
42. Pasquereau B, DeLong MR, & Turner RS (2016) Primary motor cortex of the parkinsonian monkey: altered encoding of active movement. *Brain* 139(Pt 1):127-143.
43. Mathy A*, et al.* (2009) Encoding of oscillations by axonal bursts in inferior olive neurons. *Neuron* 62(3):388-399.
44. Hansel C & Linden DJ (2000) Long-term depression of the cerebellar climbing fiber–Purkinje neuron synapse. *Neuron* 26(2):473-482.
45. Bengtsson F, Ekerot CF, & Jorntell H (2011) In vivo analysis of inhibitory synaptic inputs and rebounds in deep cerebellar nuclear neurons. *PLoS One* 6(4):e18822.
46. Hoebeek FE, Witter L, Ruigrok TJ, & De Zeeuw CI (2010) Differential olivo-cerebellar cortical control of rebound activity in the cerebellar nuclei. *Proc Natl Acad Sci U S A* 107(18):8410-8415.
47. Chorev E, Yarom Y, & Lampl I (2007) Rhythmic episodes of subthreshold membrane potential oscillations in the rat inferior olive nuclei in vivo. *J Neurosci* 27(19):5043-5052.
48. Schweighofer N, Doya K, & Kawato M (1999) Electrophysiological properties of inferior olive neurons: A compartmental model. *J Neurophysiol* 82(2):804-817.
49. Horn KM, Van Kan PL, & Gibson AR (1996) Reduction of rostral dorsal accessory olive responses during reaching. *J Neurophysiol* 76(6):4140-4151.
50. Gibson AR, Horn KM, & Pong M (2004) Activation of climbing fibers. *Cerebellum* 3(4):212-221.

51. Ohye C*, et al.* (1970) Effect of dorsal rhizotomy on postural tremor in the monkey. *Exp Brain Res* 10(2):140-150.

52. Eyre MD, Renzi M, Farrant M, & Nusser Z (2012) Setting the time course of inhibitory synaptic currents by mixing multiple GABAA receptor α subunit isoforms. *Journal of Neuroscience* 32(17):5853-5867.

53. Uusisaari M & Knopfel T (2008) GABAergic synaptic communication in the GABAergic and non-GABAergic cells in the deep cerebellar nuclei. *Neuroscience* 156(3):537-549.

54. Najac M & Raman IM (2015) Integration of Purkinje cell inhibition by cerebellar nucleo-olivary neurons. *J Neurosci* 35(2):544-549.

55. Zhang K*, et al.* (2010) Long-term results of thalamic deep brain stimulation for essential tremor. *J Neurosurg* 112(6):1271-1276.

56. Zackowski KM*, et al.* (2002) Thalamic stimulation reduces essential tremor but not the delayed antagonist muscle timing. *Neurology* 58(3):402-410.

57. Kuncel AM, Cooper SE, Wolgamuth BR, & Grill WM (2007) Amplitude- and frequency-dependent changes in neuronal regularity parallel changes in tremor With thalamic deep brain stimulation. *IEEE Trans Neural Syst Rehabil Eng* 15(2):190-197.

58. Kronenbuerger M, Gerwig M, Brol B, Block F, & Timmann D (2007) Eyeblink conditioning is impaired in subjects with essential tremor. *Brain* 130(Pt 6):1538-1551.

59. Louis ED*, et al.* (2007) Neuropathological changes in essential tremor: 33 cases compared with 21 controls. *Brain* 130(Pt 12):3297-3307.

60. Choe M*, et al.* (2016) Purkinje cell loss in essential tremor: Random sampling quantification and nearest neighbor analysis. *Mov Disord* 31(3):393-401.

61. Trillenberg P*, et al.* (2006) Eye-hand coordination in essential tremor. *Mov Disord* 21(3):373-379.

62. Wills AJ, Jenkins IH, Thompson PD, Findley LJ, & Brooks DJ (1994) Red nuclear and cerebellar but no olivary activation associated with essential tremor: a positron emission tomographic study. *Ann Neurol* 36(4):636-642.

63. Petersen KJ*, et al.* (2018) Structural and functional connectivity of the nondecussating dentato-rubro-thalamic tract. *Neuroimage* 176:364-371.

64. Schnitzler A, Munks C, Butz M, Timmermann L, & Gross J (2009) Synchronized brain network associated with essential tremor as revealed by magnetoencephalography. *Mov Disord* 24(11):1629-1635.

65. Muthuraman M*, et al.* (2012) Oscillating central motor networks in pathological tremors and voluntary movements. What makes the difference? *Neuroimage* 60(2):1331-1339.

66. Boecker H*, et al.* (1996) The effect of ethanol on alcohol-responsive essential tremor: a positron emission tomography study. *Ann Neurol* 39(5):650-658.

67. Carta M, Mameli M, & Valenzuela CF (2006) Alcohol potently modulates climbing fiber-->Purkinje neuron synapses: role of metabotropic glutamate receptors. *J Neurosci* 26(7):1906-1912.

68. Pinault D & Deschenes M (1992) The origin of rhythmic fast subthreshold depolarizations in thalamic relay cells of rats under urethane anaesthesia. *Brain Res* 595(2):295-300.

69. Roffler-Tarlov S, Beart PM, O'Gorman S, & Sidman RL (1979) Neurochemical and morphological consequences of axon terminal degeneration in cerebellar deep nuclei of mice with inherited Purkinje cell degeneration. *Brain Res* 168(1):75-95.

70. Babij R*, et al.* (2013) Purkinje cell axonal anatomy: quantifying morphometric changes in essential tremor versus control brains. *Brain* 136(Pt 10):3051-3061.

71. Louis ED*, et al.* (2018) Inferior Olivary nucleus degeneration does not lessen tremor in essential tremor. *Cerebellum & ataxias* 5(1):1.

72. Lefler Y, Yarom Y, & Uusisaari MY (2014) Cerebellar inhibitory input to the inferior olive decreases electrical coupling and blocks subthreshold oscillations. *Neuron* 81(6):1389-1400.

73. Chan-Palay V (1973) On the identification of the afferent axon terminals in the nucleus lateralis of the cerebellum. An electron microscope study. *Z Anat Entwicklungsgesch* 142(2):149-186.
74. Chan-Palay V (1973) Axon terminals of the intrinsic neurons in the nucleus lateralis of the cerebellum. An electron microscope study. *Z Anat Entwicklungsgesch* 142(2):187-206.
75. Vrieler N*, et al.* (2019) Variability and directionality of inferior olive neuron dendrites revealed by detailed 3D characterization of an extensive morphological library. *Brain Struct Funct* 224(4):1677-1695.
76. Uusisaari M & Knopfel T (2011) Functional classification of neurons in the mouse lateral cerebellar nuclei. *Cerebellum* 10(4):637-646.
77. Milosevic L*, et al.* (2018) Physiological mechanisms of thalamic ventral intermediate nucleus stimulation for tremor suppression. *Brain* 141(7):2142-2155.
78. Molnar GF*, et al.* (2005) Changes in cortical excitability with thalamic deep brain stimulation. *Neurology* 64(11):1913-1919.
79. Schuhmayer N*, et al.* (2017) Task-dependent variability of Essential Tremor. *Parkinsonism Relat Disord* 41:79-85.
80. Akemann W & Knopfel T (2006) Interaction of Kv3 potassium channels and resurgent sodium current influences the rate of spontaneous firing of Purkinje neurons. *J Neurosci* 26(17):4602-4612.
81. Garrido JA, Ros E, & D'Angelo E (2013) Spike timing regulation on the millisecond scale by distributed synaptic plasticity at the cerebellum input stage: a simulation study. *Front Comput Neurosci* 7(64):64.
82. Meijer HG*, et al.* (2011) From Parkinsonian thalamic activity to restoring thalamic relay using deep brain stimulation: new insights from computational modeling. *J Neural Eng* 8(6):066005.
83. Destexhe A, Contreras D, & Steriade M (1998) Mechanisms underlying the synchronizing action of corticothalamic feedback through inhibition of thalamic relay cells. *J Neurophysiol* 79(2):999-1016.
84. Manor Y, Rinzel J, Segev I, & Yarom Y (1997) Low-amplitude oscillations in the inferior olive: a model based on electrical coupling of neurons with heterogeneous channel densities. *J Neurophysiol* 77(5):2736-2752.
85. Torben-Nielsen B, Segev I, & Yarom Y (2012) The generation of phase differences and frequency changes in a network model of inferior olive subthreshold oscillations. *PLoS Comput Biol* 8(7):e1002580.
86. Steuber V, Schultheiss NW, Silver RA, De Schutter E, & Jaeger D (2011) Determinants of synaptic integration and heterogeneity in rebound firing explored with data-driven models of deep cerebellar nucleus cells. *J Comput Neurosci* 30(3):633-658.
87. Person AL & Raman IM (2011) Purkinje neuron synchrony elicits time-locked spiking in the cerebellar nuclei. *Nature* 481(7382):502-505.
88. McCarthy MM, Brown EN, & Kopell N (2008) Potential network mechanisms mediating electroencephalographic beta rhythm changes during propofol-induced paradoxical excitation. *J Neurosci* 28(50):13488-13504.
89. Carnevale NT & Hines ML (2006) *The NEURON book* (Cambridge University Press, Cambridge, UK ; New York) pp xix, 457 p.
90. Santaniello S*, et al.* (2015) Therapeutic mechanisms of high-frequency stimulation in Parkinson's disease and neural restoration via loop-based reinforcement. *Proc Natl Acad Sci U S A* 112(6):E586-595.
91. Bakkum DJ*, et al.* (2013) Parameters for burst detection. *Front Comput Neurosci* 7:193.

FIGURE LEGENDS

Figure 1. A) Schematic of the CCTC model. *Legend*: Blue arrows: glutamatergic excitatory connections; red arrows: GABAergic inhibitory connections; PC: Purkinje cells; DCN: deep cerebellar neurons; NO: nucleo-olivary neurons; ION: inferior olive nucleus; GrL: granular layer; RN: red nucleus; PN: pontine nucleus; IN: cerebellar interneurons; Vim: ventral intermediate nucleus of the thalamus; MC: motor cortex. **B-E)** Response of PC and DCN neurons to a depolarizing stimulus applied in the ION in the proposed network model (B, D) and in rodents *in vivo* (C, E) in normal, tremor-free conditions. A single supra-threshold (10 pA) current pulse (pulse duration: 20 ms) was applied to all ION neurons in our model (black arrows in B, D) and in the inferior olivary nucleus of the rodent (black arrows in C, E) and resulted in a burst of action potentials with amplitude adaptation (i.e., complex spike) in the PC (B, C) and an after-hyperpolarization rebound burst of action potentials in the DCN (D, E). *Inset* in B): Zoom-in of the complex spike. Images in C) and E) are reproduced under Creative Commons Attribution License from refs. (43) and (45), respectively.

Figure 2. Single unit activity of neurons in the CCTC model under normal and harmaline-induced tremor conditions. **A-H)** Raster plot of ION neurons and PCs under normal condition (A, C) and harmaline-induced tremor condition (B, D), respectively, and correspondent membrane voltage of the DCN and TC neurons (E, G: normal condition; F, H: tremor condition, respectively). Blue bars in panel E-F report the timing of action potentials fired by the NO neuron. Data in A-H) are from one instance of the CCTC model simulated over a 4,000-ms-long period. Time scales in G) and H) also apply to panels A, C, E) and B, D, F), respectively. **I-J)** Comparison between the power spectral density (PSD) of the TC neuron in the CCTC model and a tremor cell in the Vim of an ET

patient, respectively. PSD in I) is reported under normal tremor-free (blue curve) and harmaline-induced tremor conditions (red curve). PSD curves are averaged across three instances of the CCTC model, each one simulated over a 60,000-ms-long period. PSD in J) is reported for a single tremor cell in a patient with ET. Image in J) is reported with permission from ref. (31). Copyright © 2005 American Physiology Society.

Figure 3. Effects of cerebellar GABAergic dysfunctions on tremor-related neural oscillations in the CCTC model. **A)** 2-D map depicting the region of the parameter space ($\mathcal{R}$, $\tau^{PC\rightarrow DCN}$) where tremor activity in the Vim is observed along with the tremor peak frequency. The blue mark indicates parameters used to simulate normal, tremor-free conditions. The yellow circle indicates parameters used for the ET-like tremor activity analyzed in B-E), i.e., $\mathcal{R}$=0.7, $\tau^{PC\rightarrow DCN}$=12 ms). For each combination of parameters ($\mathcal{R}$, $\tau^{PC\rightarrow DCN}$), the CCTC model was simulated for 4,000 ms and the first 1,000 ms were excluded from subsequent analyses. **B-E)** Comparison between the bursting activity of DCN under harmaline-induced tremor (HAR, black bars) and GABAergic dysfunctions of the PC-DCN synapses (ET, gray bars). The burst analysis was performed as reported in SI Appendix, *SI Note 2* on data collected over 60,000-ms-long simulations. The average burst period (B), burst duration (C), inter-burst interval (D), and intra-burst discharge rate (E) are reported as mean ± S.D across three model instances. Asterisks denote significant difference (Wilcoxon rank-sum test, *P*-value $P<0.01$) between values measured under HAR and ET conditions.

Figure 4. Role of the phase of ION subthreshold oscillations in the generation of tremor-related network oscillations. **A)** In any ION neuron, the lag between an action potential and the peak of

the following subthrehsold oscillation (black asterisk) defines the duration of the oscillation cycle. The onset time T of the depolarizing input current I_{STEP} is varied between 0 (i.e., at the time of the action potential) and the peak of the subthreshold oscillation. The current is applied until an action potential is generated (red line) or the peak of the subthreshold oscillation (black line), whichever happens first. **B)** 2-D map depicting the region of the parameter space (I_{STEP}, T) where ION neurons sustain tonic spiking along with the resultant firing rate. Curves in black, pink, cyan, green, and yellow denote the region where at least 4, 5, 6, 7, or all ION neurons sustain spiking simultaneously, respectively. For each combination (I_{STEP}, T) in B), three model instances were simulated over a 4,000-ms-long period and the simulation results from the first 1,000 ms were discarded. The firing rate was measured from any ION neuron that sustained spiking until the end of simulation. **C)** The ION firing rate as a function of the duration of the current I_{STEP} for several values of the current intensity. **D)** Role of the dentato-rubro-olivary pathway in propagating tremor-related oscillations through the olivocerebellar loop. A schematic of the interconnections between ION, PC, and DCN cells mediated by di-synaptic connections through the red nucleus (RN) is provided (a) along with the simulated spiking activity of an ION neuron (black lines, panels b,c), PCs (d,e), and the DCN (f,g) under normal, tremor-free condition (b,d,f) and ET condition (i.e., yellow circle in Fig. 3A) (c,e,g). Green lines in (b,c) denote the postsynaptic glutammatergic currents to the ION neuron mediated by the RN. The red vertical lines denote the onset time for the ION neuron's action potential. This action potential elicits a complex spike in the PCs, which hyperpolarizes the DCN and causes a post-hyperpolarization rebound burst (f,g). The lag $\Delta_{ION \rightarrow DCN\_burst}$ between the ION neuron's action potential and the DCN rebound predicts whether the ION neuron will spike again and corresponds to the parameter T in A-B). Time scales in f) and g) also apply to b, d) and c, e), respectively. **E)** Histogram of the values of $\Delta_{ION \rightarrow DCN\_burst}$ measured

735 under non-tremor (blue bars) and ET conditions (red bars). For each condition, data were obtained
736 from the simulations reported in Fig. 3A above.
737
738 **Figure 5.** Effect of Vim deep brain stimulation (DBS) under cerebellar GABAergic dysfunctions.
739 **A)** Power spectral density (PSD) of Vim under ET condition (i.e., yellow circle in Fig. 3A) with
740 185-Hz DBS of the Vim (ET + Vim DBS, black line) and without Vim DBS (ET, red line). Note
741 the logarithmic scale on the axes. **B)** 2-D map depicting the region of the parameter space ($\mathcal{R}$,
742 $\tau^{PC\rightarrow DCN}$) where tonic spiking activity in the ION neurons is observed under 185-Hz-DBS of the
743 Vim along with the average ION firing rate. The red dashed lines indicate the boundary of the
744 tremor region when no DBS was applied. The upper-right region with no sustained ION firing is
745 due to overly strong DCN rebound firing, which is facilitated as a result of DBS and is not
746 compensated by the postsynaptic inhibitory currents elicited by the PC complex spikes. The PSD
747 curves in A) and the 2-D map in B) are obtained from 4,000-ms simulations of the CCTC model
748 (first 1,000 ms are discarded to let model instances reach steady-state conditions). **C)** Average
749 inter-burst interval (IBI) for the DCN in response to Vim DBS at different frequencies (black dots)
750 and least-square fourth order polynomial fit (red curve, coefficient of determination for the fitting
751 $R^2 = 0.73$). *Inset*: Coefficient of variation (CoV) of the IBI values under Vim DBS (black dots) and
752 least-square fourth order polynomial fit (red curve, $R^2=0.41$). **D)** Average firing rate of the ION
753 neurons under Vim DBS at different frequencies (black dots) and fourth order polynomial fit (red
754 curve, $R^2=0.48$). Each data point in C-D) is obtained from a 5,000-ms simulation of the CCTC
755 model (first 1,000 ms were discarded for initialization) under ET condition.
756
757 **Figure 6.** Scale-up model (i.e., 425- instead of 85-single compartment model) under normal,

tremor-free condition (A, C, E, G) and ET condition (i.e., yellow circle in Fig. 3A) (B, D, F, H), respectively. **A)** A current pulse (duration: 20 ms; amplitude: 10 pA) was applied to all 40 ION neurons simultaneously (red triangle), which led to synchronous firing of ION neurons for 2-3 cycles but no tonic spiking activity. **B)** The same current pulse as in A) was applied to 16 ION neurons simultaneously under ET condition (red triangle mark) and caused tonic spiking activities that spread to the entire ION neuron population. **C-F)** Spiking pattern of the PC, DCN and NO neurons in response to the exogenous pulse to the ION neurons in A) (C, E) and in B) (D, F), respectively. **G-H)** Power spectrogram of the Vim in response to the pulse to the ION neurons in A) (G) and in B) (H), respectively. Note that under ET condition, a prominent 7-8 Hz oscillation emerged in the spectrogram after the ION neurons were engaged into tonic spiking. Time scales in G) and H) also apply to A, C, E) and B, D, F), respectively.

Figure 1

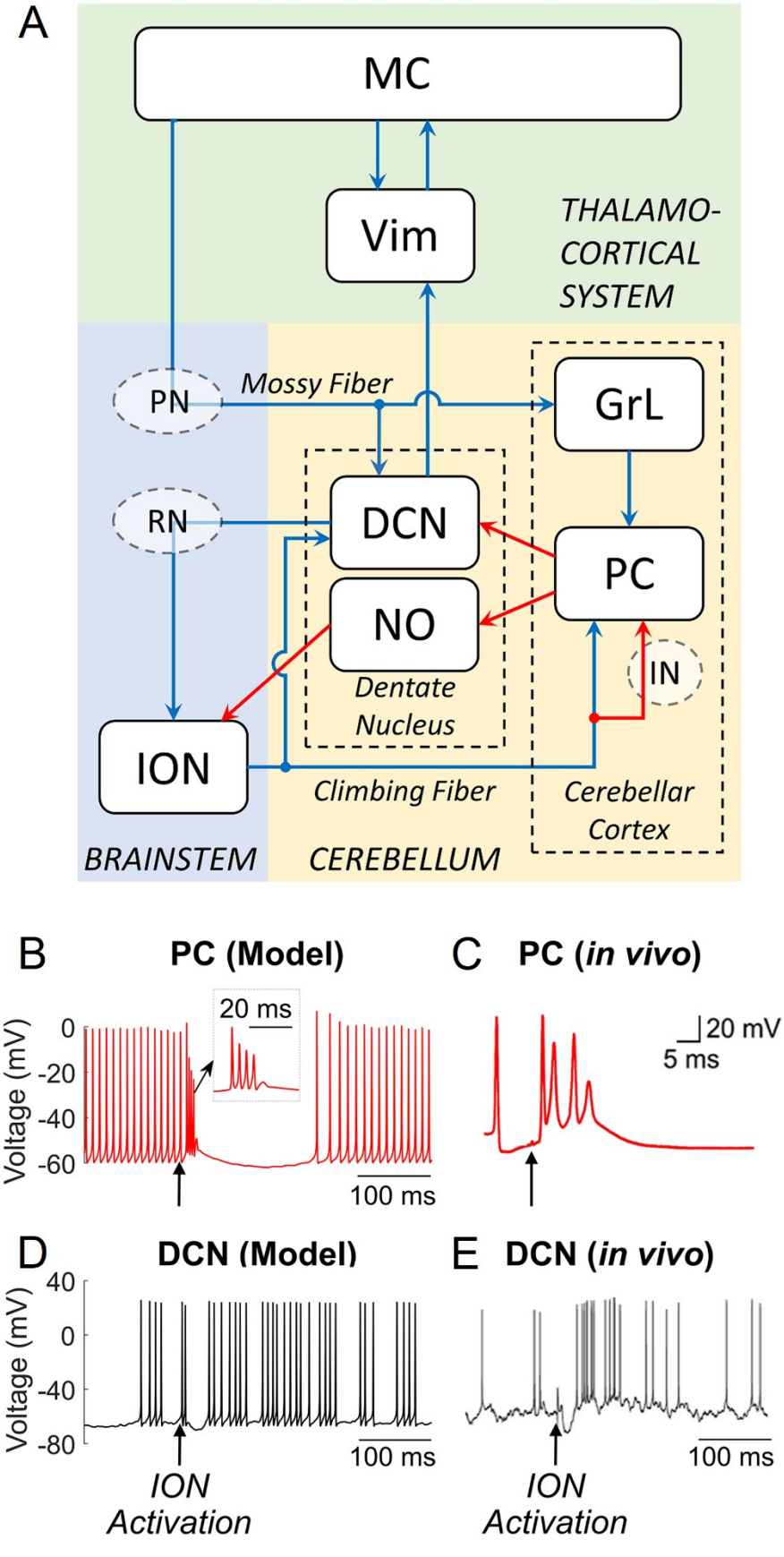
A
MC
Vim
THALAMO-
CORTICAL
SYSTEM
PN
Mossy Fiber
GrL
RN
DCN
PC
NO
IN
Dentate
Nucleus
ION
Climbing Fiber
Cerebellar
Cortex
BRAINSTEM
CEREBELLUM
B
PC (Model)
20 ms
Voltage (mV)
0
-20
-40
-60
100 ms
C
PC (in vivo)
20 mV
5 ms
D
DCN (Model)
Voltage (mV)
40
0
-40
-80
100 ms
ION
Activation
E
DCN (in vivo)
100 ms
ION
Activation

Figure 2

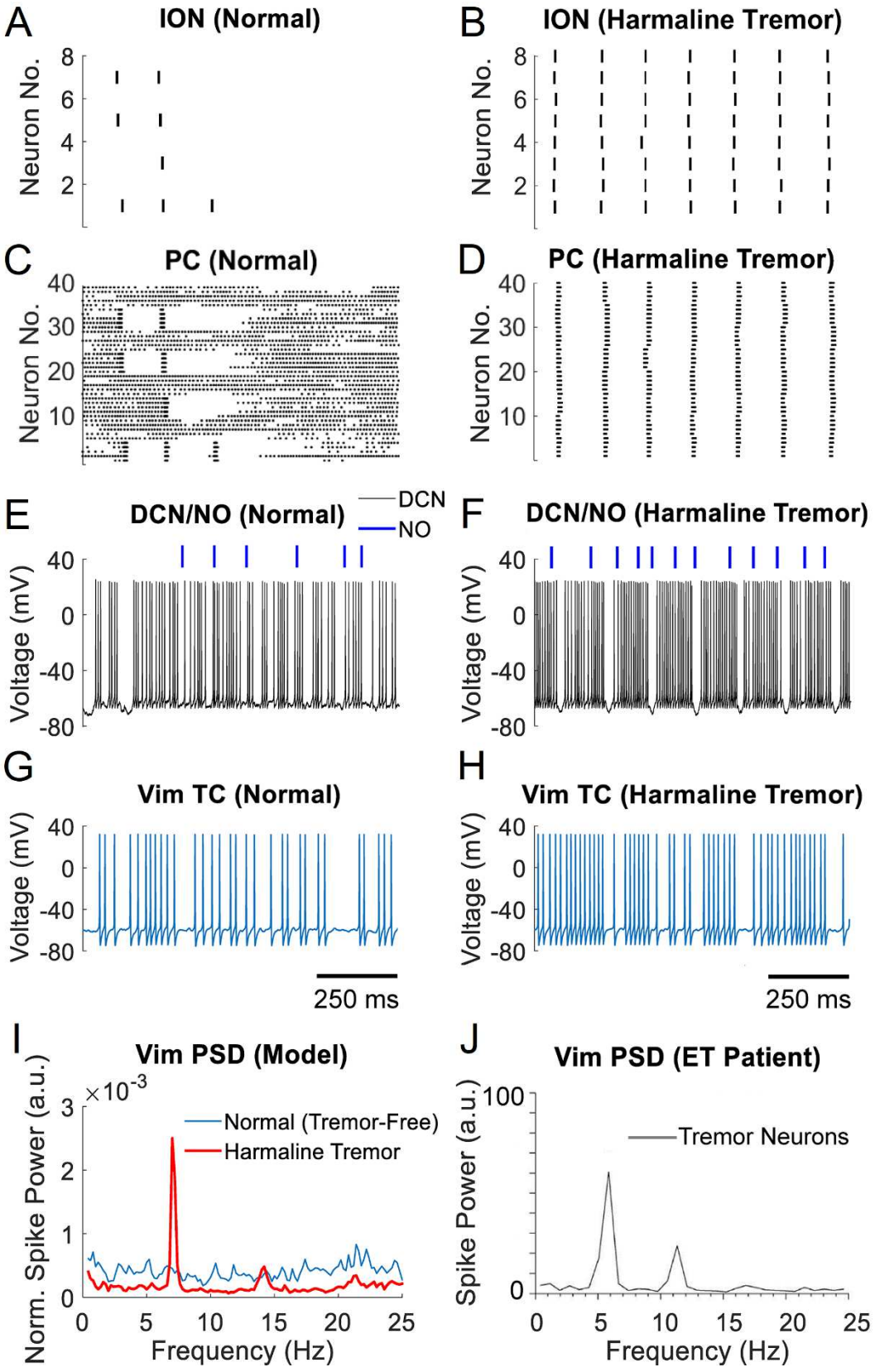
A
ION (Normal)
Neuron No.
B
ION (Harmaline Tremor)
Neuron No.
C
PC (Normal)
Neuron No.
D
PC (Harmaline Tremor)
Neuron No.
E
DCN/NO (Normal)
DCN
NO
Voltage (mV)
F
DCN/NO (Harmaline Tremor)
Voltage (mV)
G
Vim TC (Normal)
Voltage (mV)
250 ms
H
Vim TC (Harmaline Tremor)
Voltage (mV)
250 ms
I
Vim PSD (Model)
×10^-3
Normal (Tremor-Free)
Harmaline Tremor
Norm. Spike Power (a.u.)
Frequency (Hz)
J
Vim PSD (ET Patient)
Tremor Neurons
Spike Power (a.u.)
Frequency (Hz)

Figure 3

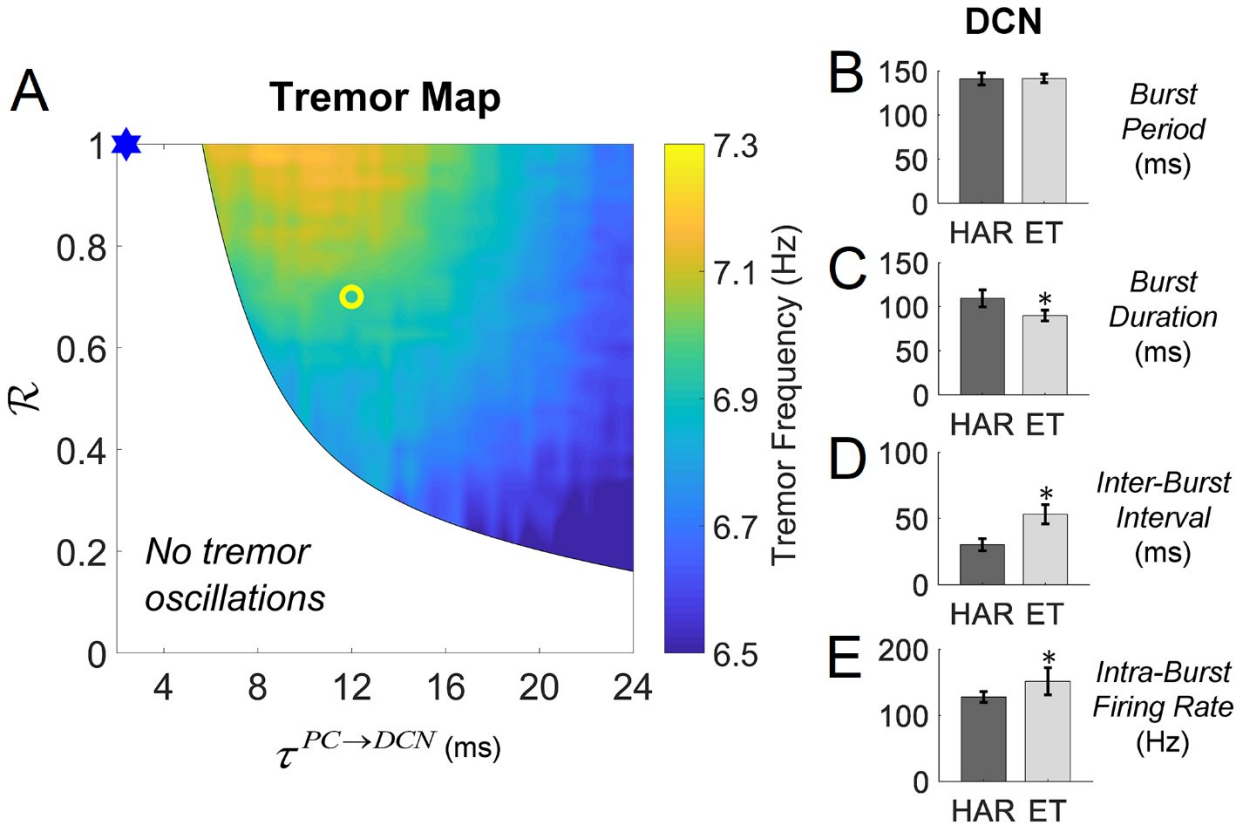
A
Tremor Map
1
0.8
0.6
0.4
0.2
0
$\mathcal{R}$
No tremor
oscillations
4
8
12
16
20
24
$\tau^{PC\rightarrow DCN}$ (ms)
7.3
7.1
6.9
6.7
6.5
Tremor Frequency (Hz)
DCN
B
150
100
50
0
HAR ET
Burst
Period
(ms)
C
150
100
50
0
*
HAR ET
Burst
Duration
(ms)
D
100
50
0
*
HAR ET
Inter-Burst
Interval
(ms)
E
200
100
0
*
HAR ET
Intra-Burst
Firing Rate
(Hz)

Figure 4

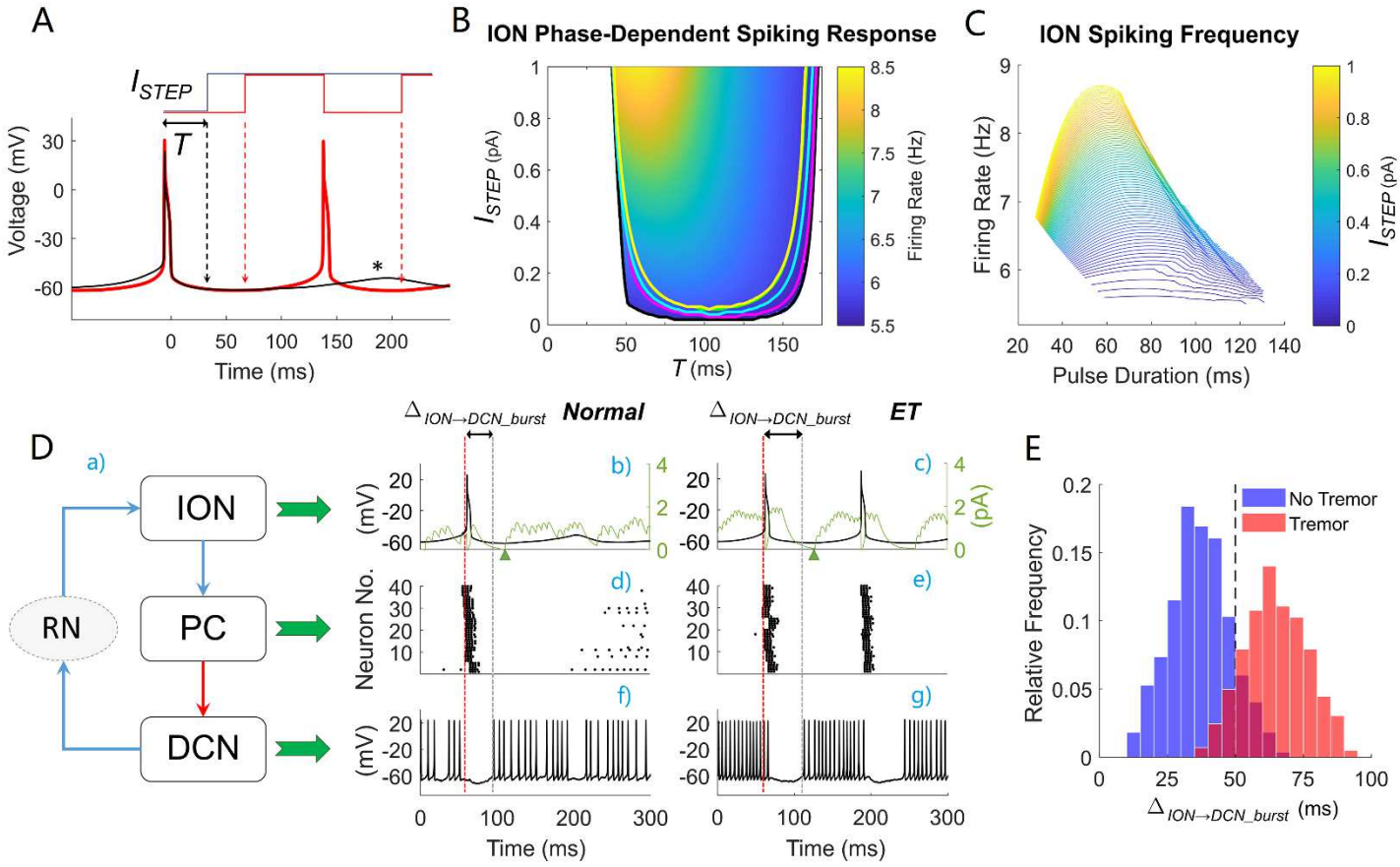
A
I_{STEP}
T
Voltage (mV)
30
0
-30
-60
0
50
100
150
200
Time (ms)
B
ION Phase-Dependent Spiking Response
I_{STEP} (pA)
T (ms)
Firing Rate (Hz)
C
ION Spiking Frequency
Firing Rate (Hz)
Pulse Duration (ms)
I_{STEP} (pA)
D
a)
ION
PC
DCN
RN
$\Delta_{ION\rightarrow DCN\_burst}$
Normal
ET
b)
c)
d)
e)
f)
g)
(mV)
(pA)
Neuron No.
Time (ms)
E
No Tremor
Tremor
Relative Frequency
$\Delta_{ION\rightarrow DCN\_burst}$ (ms)

Figure 5

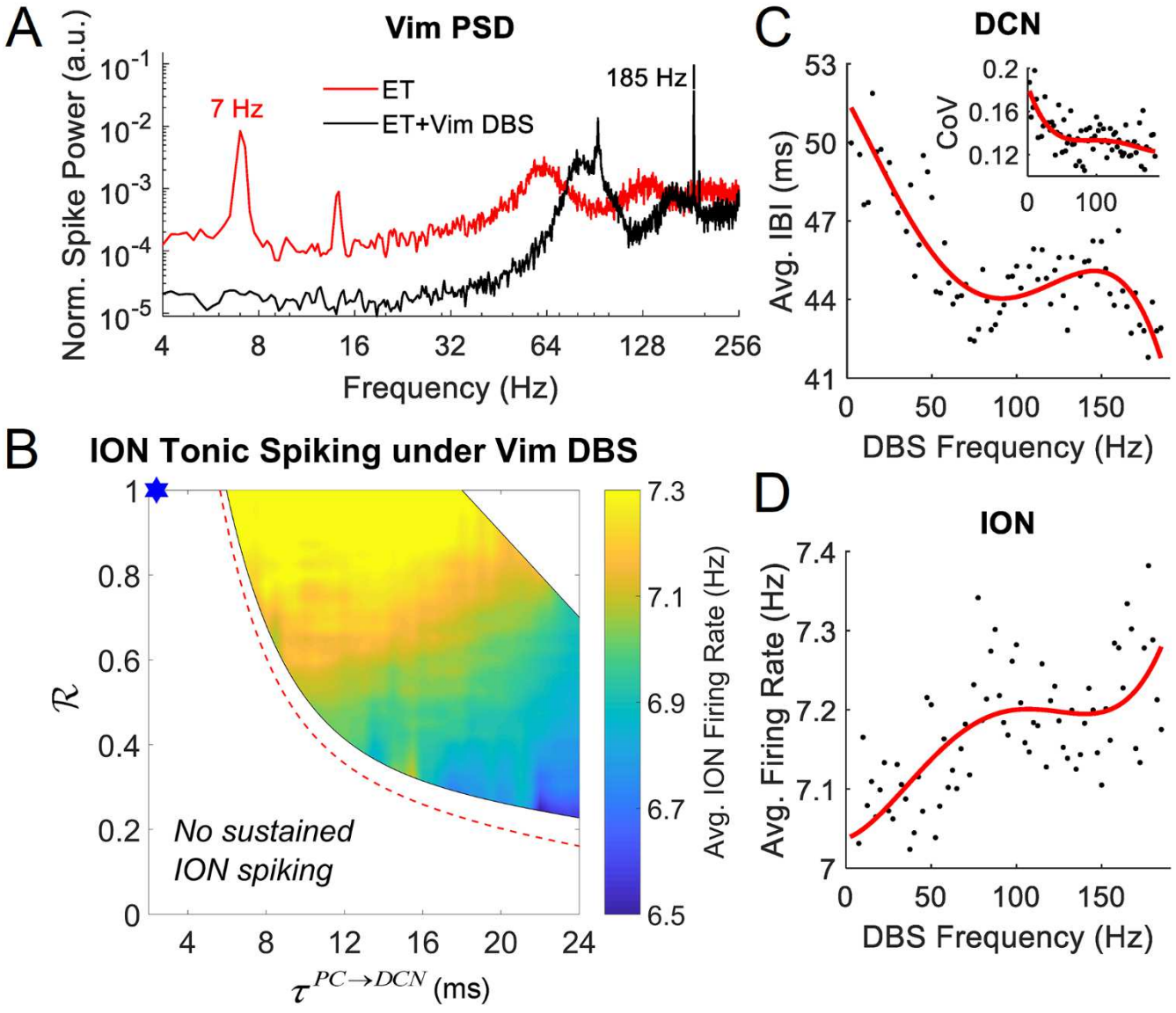
A
Vim PSD
Norm. Spike Power (a.u.)
7 Hz
185 Hz
ET
ET+Vim DBS
Frequency (Hz)
C
DCN
Avg. IBI (ms)
CoV
DBS Frequency (Hz)
B
ION Tonic Spiking under Vim DBS
No sustained
ION spiking
Avg. ION Firing Rate (Hz)
D
ION
Avg. Firing Rate (Hz)
DBS Frequency (Hz)

Figure 6

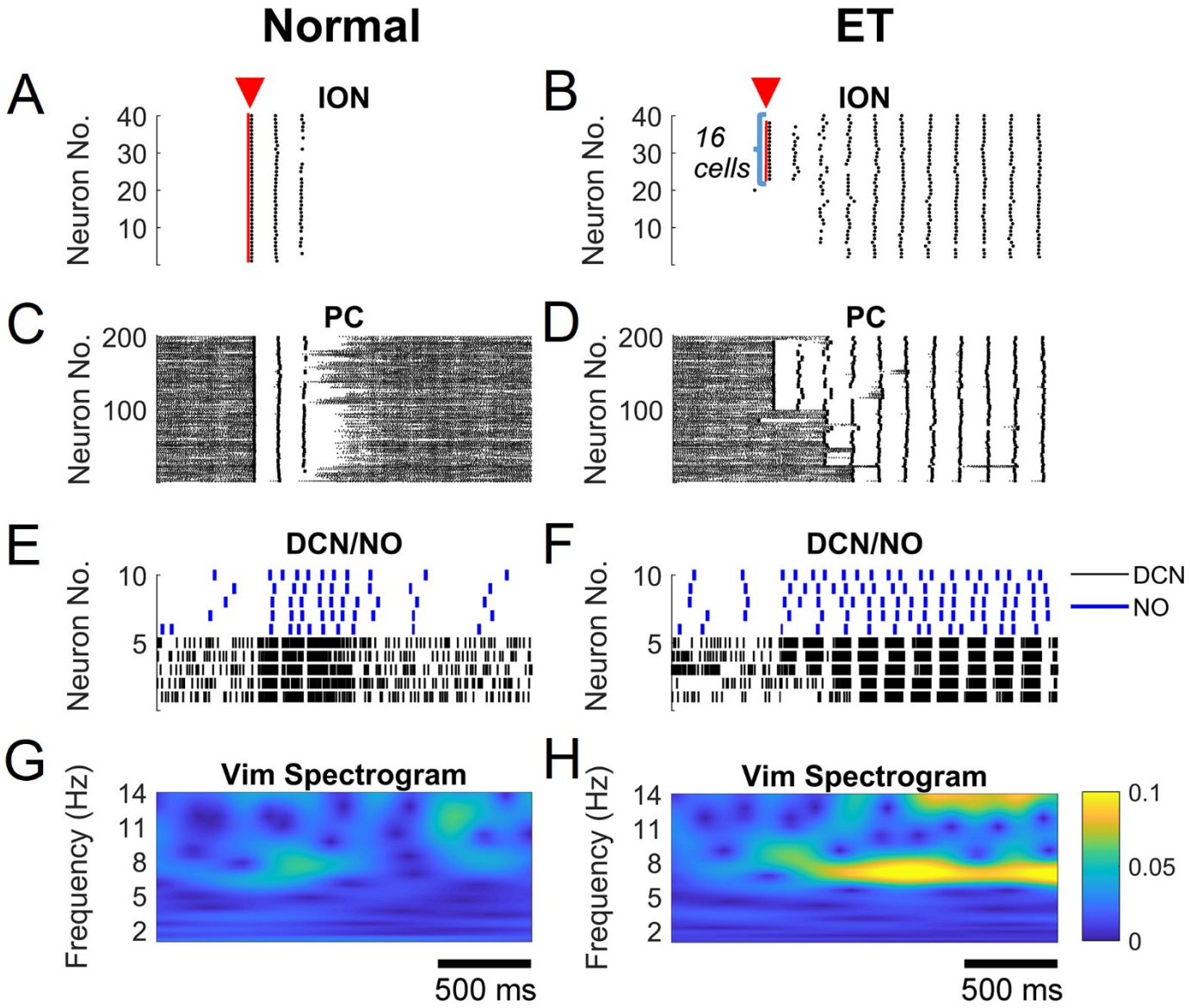
Normal
ET
A
ION
Neuron No.
40
30
20
10
B
ION
16
cells
Neuron No.
40
30
20
10
C
PC
Neuron No.
200
100
D
PC
Neuron No.
200
100
E
DCN/NO
Neuron No.
10
5
F
DCN/NO
Neuron No.
10
5
DCN
NO
G
Vim Spectrogram
Frequency (Hz)
14
11
8
5
2
500 ms
H
Vim Spectrogram
Frequency (Hz)
14
11
8
5
2
0.1
0.05
0
500 ms

Supporting Information

Role of Cerebellar GABAergic Dysfunctions in the Origins of Essential Tremor

Xu Zhang, Sabato Santaniello

Biomedical Engineering Department, University of Connecticut, Storrs, CT (USA)

SI Note 1: Mathematical Descriptions of the CCTC Network Model

The inferior olivary nucleus (ION) neuron model was modified from ref. (3) by including the somatic compartment and replacing the model of calcium channel with the model provided in refs. (4, 5). The deep cerebellar neuron (DCN) model was the somatic compartment of the original model proposed in ref. (6). The nucleo-olivary neuron (NO) model was modified from the DCN model by preserving the fast sodium current (I_{NaF}), the fast and slow delayed rectifier potassium currents (I_{fKdr} and I_{sKdr}, respectively), and the leaky channel, as in ref. (8). The equations of the remaining neuron models in the network are as in refs. (9-12). The temperature parameters, if included in the original models, were adjusted to physiological temperature (36 °C).

Each ION neuron received a different offset current (I_{OC}, *Table S1*) to generate subthreshold oscillations with slightly different intrinsic frequencies. Similarly, each Purkinje cell (PC) was endowed with a different I_{OC} to simulate a range of spontaneous firing rates. The DCN and NO neurons, the pyramidal neurons (PYN), and the fast-spiking interneurons (FSI), instead, received a constant I_{OC} specific to the neuron type to match their baseline firing rates reported in refs. (8, 12-14). For each neuron except those in the granular layer (GrL), a membrane noise $w_m(t) \sim \mathcal{N}(0, \sigma_m^2)$ was added to the capacitive current term of the Hodgkin-Huxley equation to induce a moderate level of stochasticity. A full list of the modified parameters is reported in *Table S1*. Other parameters, instead, are as reported in refs. (3, 4) (ION neurons), (9) (PCs), (6) (DCN and NO neurons), (10) (GrL neurons), (11) (thalamocortical [TC] neurons, used in Vim), and (12) (PYNs and FSIs). *Fig. S1* shows that the modified models for ION, DCN, and NO neurons matched the dynamics of neurons recorded

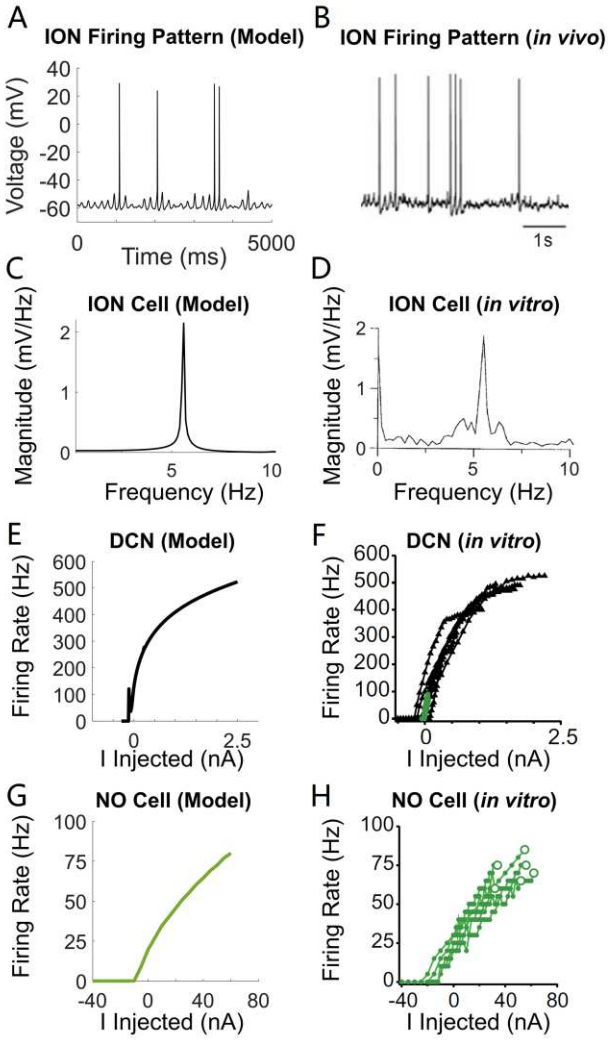

Figure S1. Single-unit activity of inferior olivary (ION), deep cerebellar (DCN), and nucleo-olivary (NO) neurons in the proposed model (A, C, E, G) and in single unit recordings from animals (B, D, F, H). **A-B)** Membrane voltage trace of a neuron in the inferior olivary nucleus under normal conditions in the model (A) and single-unit *in vivo* recording from guinea pigs (B). **C-D)** Average power spectral density (PSD) of the membrane potential of a single ION model neuron under normal, tremor-free conditions (C) (simulation: 10,000 ms) and of a single-unit *in vitro* recording in the inferior olivary nucleus of guinea pigs (D). **E-H)** Current-frequency (*I-f*) curve for DCN (E, F) and NO (G, H) neurons under a range of offset currents in the proposed model (E, G) and *in vitro* in a mouse model under anesthesia (F, H). Fig. S1B: Republished with permission of the Society for Neuroscience, from ref. (1); permission conveyed through Copyright Clearance Center, Inc. Fig. S1D: Reprinted from ref. (7), with permission from Elsevier. Fig. S1F and Fig. S1H: Republished with permission of the Society for Neuroscience, from ref. (8); permission conveyed through Copyright Clearance Center, Inc.

in animal preparations (ION: guinea pig; DCN and NO: mouse). Specifically, the ION neuron model was characterized by a sustained subthreshold oscillatory activity with frequencies ranging between 5.38 Hz and 5.78 Hz, depending on the value of I_{OC}, which matches the range of spontaneous subthreshold oscillations observed *in vitro* in slices including the ION (7), see *Fig. S1*, panels A-D. Similarly, the proposed models for DCN and NO neurons matched the *I-f* curve estimated *in vivo* in mice under anesthesia (8), *Fig. S1*, panels E-H.

Fig. S2, panels A and C, show the sample distribution of inter-spike intervals (ISI) for a Purkinje cell (PC) and the deep cerebellar neuron (DCN), respectively, in one instance of the CCTC model. Parameters of the interconnections between DCN and PCs were constrained to match the sample ISI distribution of PC and DCN recorded *in vivo* in healthy non-human primates during voluntary arm movements, see *Fig. S2*, panels B and D.

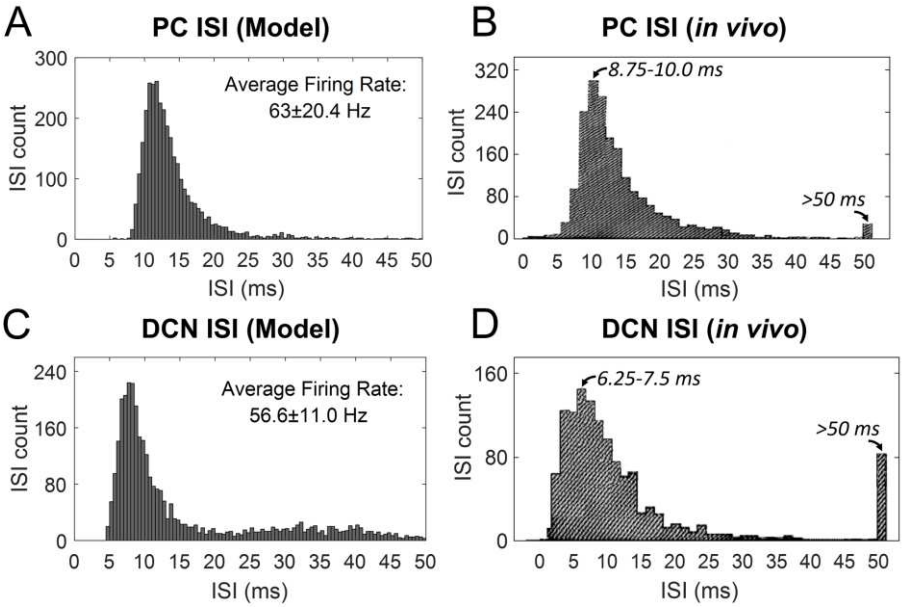

Figure S2. A-D) Inter-spike interval (ISI) distribution of one Purkinje cell (PC) and one deep cerebellar neuron (DCN) in the CCTC model (A, C) and in awake nonhuman primates (B, D) during upper limb movements. Histograms in A) and C) are from one instance of the CCTC model simulated over a 60,000-ms-long period. *Inset*: Average firing rate (mean ± S.D.) of the PCs and DCNs, respectively, across three instances of the CCTC model, each instance simulated over a 60,000-ms-long period. Fig. S2B and Fig. S2D: Reprinted with permission from ref. (2); permission conveyed through Copyright Clearance Center, Inc.

Network Connectivity. A simplified representation of the thalamocortical pathway is included in our model, with one thalamocortical (TC) neuron in the Vim projecting onto six, randomly chosen PYNs and both FSIs, and four PYNs projecting back to the TC neuron. In addition, four, randomly chosen PYNs project individually onto four identical GrL structures, representing the relay of cortical inputs to the cerebellum via pontine nuclei (15). All PYNs project onto the DCN to simulate the formation of extensive mossy fiber excitation, as reported in ref. (16). The NO neuron model, instead, does not receive excitatory input from the PYNs to account for the low *in vivo* firing activity of the nucleo-olivary neurons (17, 18). Also, a total of 8 out of 20 PYNs are neither involved in connections with the Vim nor with the cerebellar cortex and are used to account for the important fact that thalamocortical and cortico-cerebellar projections may target different cortical layers. Each ION neuron projects onto five PCs without overlapping as reported in ref. (19). One of the IONs projects onto the DCN to account for the presence of climbing fiber collaterals. These collaterals are known to produce small, short-latency activation of DCN neurons following a spike of the ION neurons (13, 20, 21).

Fig. S3 on next page reports the interconnections between ION neurons in the inferior olivary nucleus (*Fig. S3*, panel A), the motor cortex (*Fig. S3*, panel B), and the neurons forming the granular layer (GrL complex) in the cerebellar cortex (*Fig. S3*, panel C). The topology of the resultant neuronal networks is consistent with anatomical considerations reported in ref. (10). The olivocerebellar pathway formed by PCs, NO, and ION neurons represents a loop, as indicated in ref. (22), and the di-synaptic excitatory pathway from the DCN to the ION neurons, i.e., the dentato-rubro-olivary pathway, is organized to form the Guillain-Mollaret triangle (23).

Synapses between the granule cells, Golgi cells, and stellate cells in the GrL complex were modeled as in ref. (8). Synapses within the motor cortex as well as those between the PCs and DCN or NO neurons, instead, were modeled as follows:

$$I_{syn} = g_{syn} s\left(V_i(t) - E_{syn}\right) \tag{1}$$

$$\frac{ds}{dt} = \alpha\left[1 + \tanh\left(\frac{V_j(t-\Delta t) - V_{off}}{\beta}\right)\right](1-s) - \frac{s}{\tau} + w_s(t) \tag{2}$$

where $V_j(t - \Delta t)$ is the membrane potential of the pre-synaptic neuron at time $(t - \Delta t)$ and Δt accounts for the synaptic transmission delay. The term $w_s(t)$ represents synaptic noise and is defined by:

$$\frac{dw_s(t)}{dt} = S, S \sim \mathcal{N} \tag{3}$$

where $\mathcal{N}$ is a Gaussian distribution with mean 0 and standard deviation σ_s. For the motor cortex, V_{off}=0 mV, β=4, Δt=0, and the rest of the parameters were set as described in ref. (24). For the synapses between PCs and DCN or NO neurons, the parameters are reported in *Table S2*.

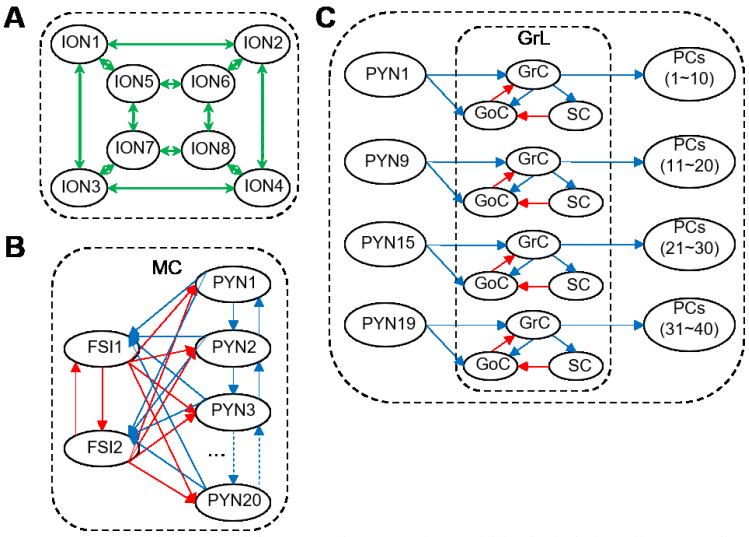

Figure S3. **A-C)** Schematic of the network connections within the inferior olivary nucleus (A), the motor cortex [MC] (B), and the granular layer [GrL] (C). Green arrows in A) indicate electric gap junctions, whereas blue and red arrows in B-C) indicate glutamatergic excitatory and GABAergic inhibitory connections, respectively. Arrow tips indicate post-synaptic neurons.

All the remaining synapses along the CCTC loop were simulated in NEURON using the NETCON mechanism, which produces an event-based post-synaptic current upon detection of a presynaptic spike, and speeds up the simulation (25). NETCON mechanisms were specifically used to model the di-synaptic connections DCN→ ION, PYN→DCN, and PYN→GrL, as well as the di-synaptic inhibitory connection between ION neurons and PCs mediated by cerebellar interneuron (26). A NETCON mechanism works as follows: denoted with i and j the post-synaptic target neuron and the pre-synaptic neuron, respectively, NETCON delivers a post-synaptic current I_{syn} to the target neuron i in response to the occurrence of a spike in the pre-synaptic neuron j. The current I_{syn} is either an exponentially decaying current of form:

$$I_{syn} = g_{syn}\left(e^{-(t-\Delta t)/\tau^{j\to i}} + w_s(t)\right)\left(V_i - E_{syn}\right) \tag{4}$$

or a two-state exponentially decaying current of form:

$$I_{syn} = \frac{A \cdot g_{syn}}{\tau_2^{j\to i} - \tau_1^{j\to i}}\left[\left(e^{-(t-\Delta t)/\tau_2^{j\to i}} - e^{-(t-\Delta t)/\tau_1^{j\to i}}\right) + w_s(t)\right]\left(V_i - E_{syn}\right) \tag{5}$$

where Δt is the synaptic transmission delay from neuron j to neuron i, E_{syn} is the synaptic reverse potential, V_i is the postsynaptic membrane potential in neuron i, g_{syn} is the postsynaptic conductance, and $\tau_k{}^{j\to i}$, k=1, 2, are decay time constants, respectively. A spike was detected in the pre-synaptic neuron j if the voltage V_j passed the threshold thr= –40 mV (–50 mV for Golgi cells).

To simulate the spontaneous discharge activity of the pyramidal neurons in the motor cortex, each PYN received post-synaptic currents triggered by a train of randomly generated pre-synaptic spikes (Poisson process). The parameter λ of the Poisson processes (i.e., average inter-event interval) was randomly generated (one Poisson process per PYN) according to a Gaussian distribution, i.e., $\lambda \sim \mathcal{N}(\mu, \sigma^2)$ with μ=20 ms and σ=5 ms. Similarly, the spontaneous discharge activity of the ION neurons was simulated by delivering post-synaptic currents to these neurons in response to a train of randomly generated pre-synaptic spikes (Poisson process). The parameter λ of the Poisson processes was randomly generated (one Poisson process per ION) and followed a uniform distribution, i.e., $\lambda \sim \mathcal{U}(350, 650)$ ms, to match experimental data in ref. (27). All the parameters used in the synapses in our model are reported in *Table S2*.

Each ION neuron was connected to three additional ION neurons via gap junctions to reproduce quantitative neuroanatomical indications reported ref. (27), see *Fig. S3*, panel A. Each gap junction was simulated as a linear function of the membrane potential difference between the connected ION neurons, i.e.,

$$I_{gap} = g_{gap}\gamma_C\left(V_i - V_j\right) \tag{6}$$

where γ_C is a coupling coefficient, g_{gap} is the gap junction conductance, and V_i and V_j are the membrane potential of the target cell i and the cell j in electrotonic contact with the target cell. The conductance g_{gap} was normally distributed across the gap junctions in the model with values drawn from the distribution function $\mathcal{N}(\mu, \sigma^2)$ with parameters μ=2.25×10^{-5} mS/cm^2 and σ=1.0×10^{-5} mS/cm^2 to match data in ref. (27).

The coupling coefficient γ_C was defined as a scalar ranging between 0 and 1 and was used to describe the effects of the nucleo-olivary activity onto the inferior olivary neurons. It has been reported, in fact, that the NO neurons project onto both the soma and the gap junctions of the ION neurons, which results in a strong decoupling between the ION neurons and a significant hyperpolarization of the ION somas (27). To account for the effects of the NO neurons onto the gap junctions, we modeled the coefficient γ_C as a function of the spiking of the NO neuron, i.e.:

$$\gamma_C = 1 - 0.9\tanh\left(S(t)\right) \tag{7}$$

where $S(t)$ is a two-state exponential function of the NO spiking time, i.e.:

$$S(t) = \frac{A \cdot s}{\tau_2 - \tau_1}\left(e^{-t/\tau_2} - e^{-t/\tau_1}\right). \tag{8}$$

Specific parameters for the gap junctions are reported in *Table S2*. The innervation of the climbing fibers to the Purkinje cells (PCs) was simulated by introducing AMPA-mediated and NMDA-mediated glutamatergic synapses on the PCs. The values of these currents match the synaptic currents reported in refs. (28-31). The interneuron-mediated inhibitory effects of the ION spiking onto the PCs (26) were modeled through a NETCON mechanism (parameters are in *Table S2*). *Fig. S4* on next page illustrates the spiking pattern of the neuron models in the proposed CCTC loop before and after the application of a single, depolarizing impulse to the ION neurons (red vertical line). Neurons from the motor cortex (PYNs and FSIs) were mildly affected by the GABAergic disfunctions in cerebellum (*Fig. S4*, panels A-B). PCs and GrL neurons, instead, responded tonically to the simultaneous activation of the ION neurons. This activation was triggered externally (red vertical line) and engaged a single response under normal, tremor-free conditions (*Fig. S4*, panels C and E). Under ET conditions, instead, the simultaneous activation of the ION neurons elicited a sustained oscillation that outlasted the effects of the impulse and spread through all the cerebellar neurons, see *Fig. S4*, panels D and F. The ET conditions correspond to the GABAergic dysfunctions simulated in Fig. 3B-E in the main text, i.e., $\mathcal{R}$=0.7 and $\tau^{PC\rightarrow DCN}$=12 ms.

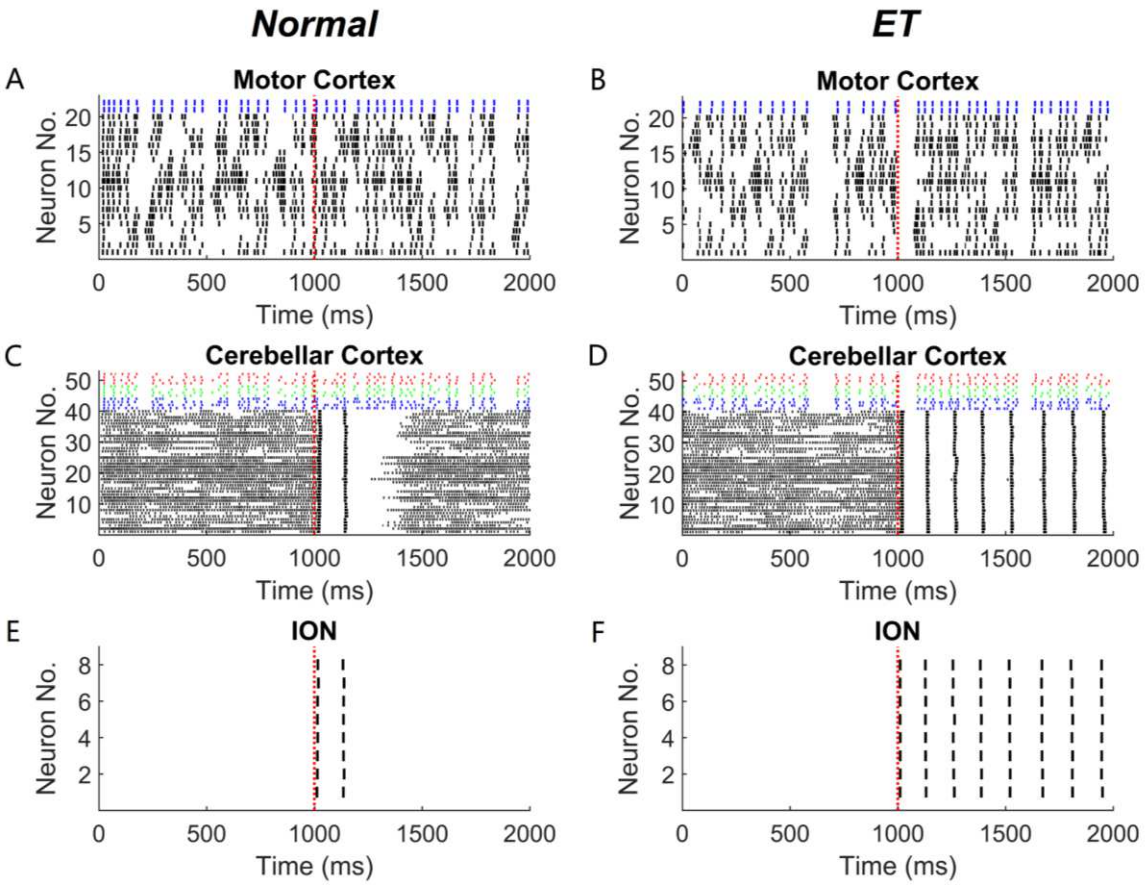

Figure S4. Raster plot of neural populations under normal, tremor-free conditions (A, C, E) and essential tremor (ET) conditions (B, D, F). **A-B)** Raster plot of neuron models from the motor cortex (black: PYNs; blue: FSIs); **C-D)** Raster plot of neuron models from the cerebellar cortex (black: Purkinje cells; blue: Golgi cells; green: granule cells; red: stellate cells. **E-F)** Raster plot of olivary neuron models from the inferior olivary nucleus. In each plot, the red dotted vertical line identifies the time t=1,000 ms when a single supra-threshold (10 pA) current pulse (pulse duration: 20 ms) was applied to all neurons in the inferior olivary nucleus. The CCTC model was simulated for 4,000 ms, integration step: 0.0125 ms.

SI Note 2: Data Analysis

The two-dimensional maps reported in Fig. 3A and Fig. 5B in the main text, and *Fig. S5* on next page were computed from 10,000-ms simulations of three instances of the model with different random seeds for each combination ($\mathcal{R}$, $\tau^{PC\rightarrow DCN}$) obtained by varying $\mathcal{R}$ between 0 and 1 with 0.025 increments and $\tau^{PC\rightarrow DCN}$ between 2.0 ms and 24 ms with 0.5 ms increments. A total of 1,800 grid points ($\mathcal{R}$, $\tau^{PC\rightarrow DCN}$) were considered. The boundaries of the tremor regions were fitted by the sum of two exponential functions. Finally, a 5-point moving average filter was implemented both horizontally and vertically to smooth the maps. Similarly, the two-dimensional map reported in Fig. 4B in the main text was computed for every pair of parameters (I_{STEP}, T), with I_{STEP} ranging between 0.01 pA and 1 pA (resolution: 0.01 pA) and T ranging between 10 ms and 180 ms (resolution: 1 ms), thus resulting in 17,100 grid points. For each parameter pair, three model instances were simulated for 6,000 ms and the ION spiking rate was calculated as the average firing rate of any ION that sustained spiking over the entire simulation period.

Rate, Burst, and Power Spectral Analyses. The firing rates of individual neurons reported in section 2.1 in the main text and *Fig. S2* (insets) were calculated from three model instances, each one simulated over a simulation period of 60,000 ms under normal tremor-free condition (the first 1,000 ms was discarded to let the network model reach steady-state conditions). The firing rates were reported as mean ±

S.D. evaluated over non-overlapping 1,000-ms-long segments of simulated data. In the subsequent analyses, a burst was defined as a group of at least three consecutive spikes with inter-spike interval no more than 30 ms. The burst detection was implemented using the method in ref. (32).

The power spectral density (PSD) of the neurons in Fig. 2E in the main text was computed from spike trains recorded over 60,000-ms-long simulations. Spike trains were sampled at 800 Hz and the PSD was computed using the Welch's method as average over 4,000-ms-long windows (Hanning window, 2,000-ms overlap). Three model instances were simulated and the resultant thalamocortical spike trains were used.

The power spectrogram in Fig. 6A and Fig. 6H in the main text were computed via wavelet decomposition (Morlet wavelet) on the superposition of the spike trains of 5 TC neurons in the Vim.

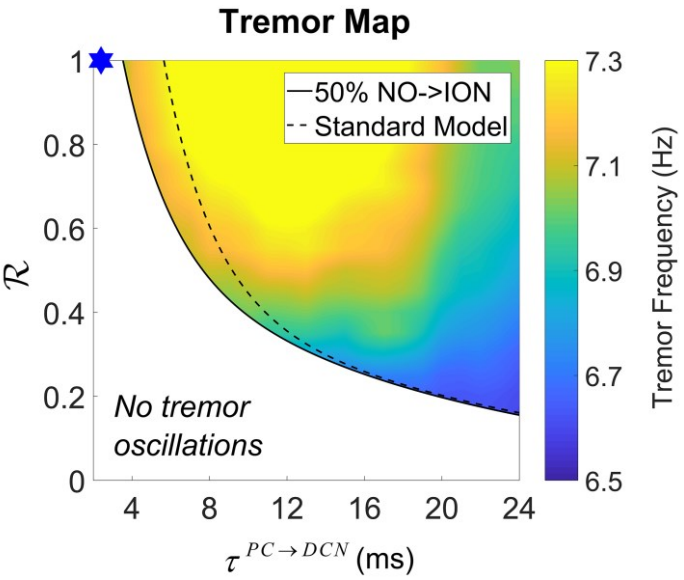

Figure S5. 2-D map depicting the region of the parameter space ($\mathcal{R}$, $\tau^{PC\rightarrow DCN}$) where tremor activity in the Vim is observed along with the tremor frequency (colormap). The tremor frequency was defined as the frequency of maximum power spectrum density of the Vim, and the blue mark indicates parameters used to simulate normal, tremor-free conditions. The synaptic strength of the NO→ION synapses in this figure was reduced to 50% of the original value used in Fig. 3A in the main text. The dashed line indicates the boundary of the tremor map reported in Fig. 3A in the main text for the original model (*Standard Model*). Note that the average tremor frequency increased by ~0.3 Hz across the entire map over the value in Fig. 3A.

SI Note 3: Connectivity of the Scale-Up Version of the CCTC Model

The 85-single compartment CCTC model was scaled up by a factor 5, i.e., the number of single compartment neurons in each neural population represented in the model was increased five times, thus resulting in a 425-single compartment CCTC model, which included 40 ION neurons, 200 PCs, 5 DCN and 5 NO neurons, 5 TC neurons in the Vim, 100 PYNs, 10 FSIs, and 20 GrL clusters altogether. Three instances of this scaled-up CCTC model were simulated with different random seeds. For each instance, the following rules were used to randomize the connectivity between the thalamocortical and olivocerebellar systems:

1) The ION neurons were divided in 5 groups (i.e., 8 neurons per group), each group forming a closed ring as depicted in *Fig. S3*, panel A. Four out of 8 ION neurons in each group formed gap junctions with ION neurons from neighboring instances, 2 on each side. For instance, ION neurons 1 and 3 in one group formed gap junctions with ION neurons 2 and 4, respectively, from a neighboring group, and vice versa. The gap junction conductance g_{gap} was increased by 50% to compensate for the more extensive inter-group connections. ION neurons in one group shared the same presynaptic Poisson process source input, see PP→ION synapses in *Table S2*;

2) Each group of ION neurons cumulatively targeted M PCs, where $30 \leq M \leq 50$ and M was drawn from a Gaussian distribution function with mean μ=40 and S.D. σ=4. Within an ION group, each ION neuron projected simultaneously onto K randomly chosen PCs out of the M PCs, where the value K was drawn from a Gaussian distribution with mean μ=5 and S.D. σ=2. This guaranteed that every ION neuron projected onto a different number K of PCs, with $1 \leq K \leq 10$;

3) Every DCN in the model received GABAergic projections from W out of 200 PCs, where the value

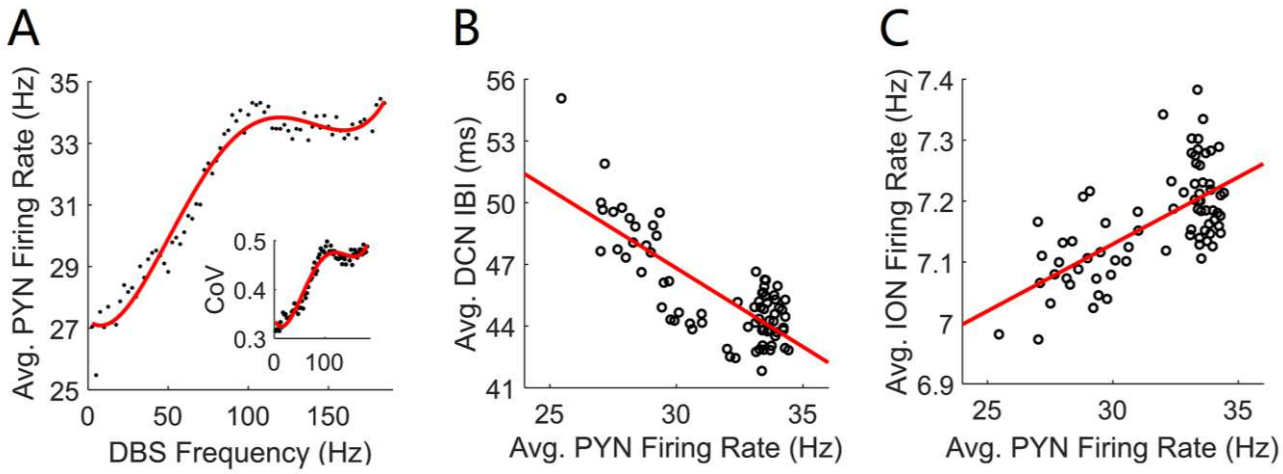

Figure. S6. A) Average firing rate for the pyramidal neurons (PYNs) in response to Vim DBS at different frequencies (black circles) and the least-square fourth order polynomial fit (red curve, coefficient of determination for the fitting R^2=0.96). *Inset*: Coefficient of variation (CoV) of the PYN firing rates in response to the Vim DBS (black dots) and least-square fourth order polynomial fit (red curve, R^2=0.95). **B-C)** Linear regressor (red line) estimated for the average DCN inter-burst intervals (R^2=0.61) (B) and the average ION firing rate (R^2=0.43) (C) as a function of the average PYN firing rate under Vim DBS from A) (black circles). Each data point in A-C) was obtained from a 5,000-ms simulation of the CCTC model under the ET condition with parameters $\mathcal{R}$=0.7 and $\tau^{PC\rightarrow DCN}$=12 ms. First 1,000 ms were discarded to let model instances reach steady-state conditions.

W was drawn from a Gaussian distribution with mean μ=40 and S.D. σ=4 for every DCN. This guaranteed that every DCN received from a different number W of PCs, with $30 \leq W \leq 50$ PCs. Each NO neuron, instead, received GABAergic inputs from 40 PCs. The Purkinje cells projecting onto a DCN or NO neuron were selected randomly.

4) Every DCN projected di-synaptically onto W_1 out of 40 ION neurons chosen randomly, where W_1 was drawn from a Gaussian distribution with mean μ=40 and S.D. σ=4 and varied for every DCN. In this way, we maximized the inter-loop connections by allowing that ION neurons from different groups may receive from the same DCN;

5) Every DCN cell projected onto a TC neuron in the Vim (ratio 1:1); every TC neuron projected onto 6 PYNs and received glutamatergic inputs from 4 PYNs with no overlapping;

6) Every PYN formed glutamatergic projections with 5 neighboring PYNs. The synaptic strength g_{syn} of the PYN→PYN connections was reduced to 20% of the original value reported in *Table S2* to accommodate for the increased number of projections. Each FSI received glutamatergic inputs from all 100 PYNs, and GABAergic inputs from the remaining 9 FSIs. Similarly, the synaptic strengths g_{syn} of the PYN→FSI and FSI→FSI connections were reduced to 20% and 11.1% of the original values reported in *Table S2*, respectively. Finally, the FSIs formed GABAergic projections onto all 100 PYNs, and the synaptic strength g_{syn} of the FSI→PYN connections was reduced to 10% of the original value in *Table S2*;

7) Every DCN received glutamatergic inputs from 20 randomly chosen PYNs. Similarly, every GrL complex received inputs from 4 randomly chosen PYNs without overlapping and projected onto 10 PCs. The PYNs projecting onto the GrL or DCN neurons did not necessarily receive input from the TC neurons in the Vim;

8) To reflect the heterogeneous properties across the 200 PC→DCN synapses, we modeled the normal, tremor-free condition by setting the parameters $\tau^{PC\rightarrow DCN} \sim \mathcal{N}(\mu, \sigma^2)$, μ=2.4 ms, σ=0.4 ms, and $\mathcal{R} \sim \mathcal{N}(\mu, \sigma^2)$, μ=1, σ=0.2, and we modeled the ET condition by setting $\tau^{PC\rightarrow DCN} \sim \mathcal{N}(\mu, \sigma^2)$, μ=12 ms, σ=2 ms, and $\mathcal{R} \sim \mathcal{N}(\mu, \sigma^2)$, μ=0.7, σ=0.14.

SI References.

1. Chorev E, Yarom Y, & Lampl I (2007) Rhythmic episodes of subthreshold membrane potential oscillations in the rat inferior olive nuclei in vivo. *J Neurosci* 27(19):5043-5052.
2. Thach WT (1968) Discharge of Purkinje and cerebellar nuclear neurons during rapidly alternating arm movements in the monkey. *J Neurophysiol* 31(5):785-797.
3. Schweighofer N, Doya K, & Kawato M (1999) Electrophysiological properties of inferior olive neurons: A compartmental model. *J Neurophysiol* 82(2):804-817.
4. Manor Y, Rinzel J, Segev I, & Yarom Y (1997) Low-amplitude oscillations in the inferior olive: a model based on electrical coupling of neurons with heterogeneous channel densities. *J Neurophysiol* 77(5):2736-2752.
5. Torben-Nielsen B, Segev I, & Yarom Y (2012) The generation of phase differences and frequency changes in a network model of inferior olive subthreshold oscillations. *PLoS Comput Biol* 8(7):e1002580.
6. Steuber V, Schultheiss NW, Silver RA, De Schutter E, & Jaeger D (2011) Determinants of synaptic integration and heterogeneity in rebound firing explored with data-driven models of deep cerebellar nucleus cells. *J Comput Neurosci* 30(3):633-658.
7. Lampl I & Yarom Y (1997) Subthreshold oscillations and resonant behavior: two manifestations of the same mechanism. *Neuroscience* 78(2):325-341.
8. Najac M & Raman IM (2015) Integration of Purkinje cell inhibition by cerebellar nucleo-olivary neurons. *J Neurosci* 35(2):544-549.
9. Akemann W & Knopfel T (2006) Interaction of Kv3 potassium channels and resurgent sodium current influences the rate of spontaneous firing of Purkinje neurons. *J Neurosci* 26(17):4602-4612.
10. Garrido JA, Ros E, & D'Angelo E (2013) Spike timing regulation on the millisecond scale by distributed synaptic plasticity at the cerebellum input stage: a simulation study. *Front Comput Neurosci* 7(64):64.
11. Meijer HG*, et al.* (2011) From Parkinsonian thalamic activity to restoring thalamic relay using deep brain stimulation: new insights from computational modeling. *J Neural Eng* 8(6):066005.
12. Destexhe A, Contreras D, & Steriade M (1998) Mechanisms underlying the synchronizing action of corticothalamic feedback through inhibition of thalamic relay cells. *J Neurophysiol* 79(2):999-1016.
13. Najac M & Raman IM (2017) Synaptic excitation by climbing fibre collaterals in the cerebellar nuclei of juvenile and adult mice. *J Physiol* 595(21):6703-6718.
14. Raman IM, Gustafson AE, & Padgett D (2000) Ionic currents and spontaneous firing in neurons isolated from the cerebellar nuclei. *J Neurosci* 20(24):9004-9016.
15. Sasaki K, Kawaguchi S, Shimono T, & Prelevic S (1970) Electrophysiological studies of the pontine nuclei. *Brain Res* 20(3):425-438.
16. Wu Y & Raman IM (2017) Facilitation of mossy fibre-driven spiking in the cerebellar nuclei by the synchrony of inhibition. *J Physiol* 595(15):5245-5264.
17. Bazzigaluppi P, Ruigrok T, Saisan P, De Zeeuw CI, & de Jeu M (2012) Properties of the nucleo-olivary pathway: an in vivo whole-cell patch clamp study. *PLoS One* 7(9):e46360.
18. Uusisaari M & De Schutter E (2011) The mysterious microcircuitry of the cerebellar nuclei. *J Physiol* 589(Pt 14):3441-3457.
19. Eccles JC, Llinas R, & Sasaki K (1966) The excitatory synaptic action of climbing fibres on the Purkinje cells of the cerebellum. *J Physiol* 182(2):268-296.
20. Hoebeek FE, Witter L, Ruigrok TJ, & De Zeeuw CI (2010) Differential olivo-cerebellar cortical control of rebound activity in the cerebellar nuclei. *Proc Natl Acad Sci U S A* 107(18):8410-8415.
21. Lu H, Yang B, & Jaeger D (2016) Cerebellar Nuclei Neurons Show Only Small Excitatory Responses to Optogenetic Olivary Stimulation in Transgenic Mice: In Vivo and In Vitro Studies. *Front Neural Circuits* 10:21.

22. Bengtsson F & Hesslow G (2006) Cerebellar control of the inferior olive. *Cerebellum* 5(1):7-14.

23. Murdoch S, Shah P, & Jampana R (2016) The Guillain-Mollaret triangle in action. *Pract Neurol* 16(3):243-246.

24. Santaniello S*, et al.* (2015) Therapeutic mechanisms of high-frequency stimulation in Parkinson's disease and neural restoration via loop-based reinforcement. *Proc Natl Acad Sci U S A* 112(6):E586-595.

25. Hines ML & Carnevale NT (2004) Discrete event simulation in the NEURON environment. *Neurocomputing* 58:1117-1122.

26. Mathews PJ, Lee KH, Peng Z, Houser CR, & Otis TS (2012) Effects of climbing fiber driven inhibition on Purkinje neuron spiking. *J Neurosci* 32(50):17988-17997.

27. Lefler Y, Yarom Y, & Uusisaari MY (2014) Cerebellar inhibitory input to the inferior olive decreases electrical coupling and blocks subthreshold oscillations. *Neuron* 81(6):1389-1400.

28. Otis TS, Kavanaugh MP, & Jahr CE (1997) Postsynaptic glutamate transport at the climbing fiber-Purkinje cell synapse. *Science* 277(5331):1515-1518.

29. Burroughs A*, et al.* (2017) The dynamic relationship between cerebellar Purkinje cell simple spikes and the spikelet number of complex spikes. *J Physiol* 595(1):283-299.

30. Murphy JT & Sabah NH (1970) The inhibitory effect of climbing fiber activation on cerebellar purkinje cells. *Brain Res* 19(3):486-490.

31. Zucca R, Rasmussen A, & Bengtsson F (2016) Climbing Fiber Regulation of Spontaneous Purkinje Cell Activity and Cerebellum-Dependent Blink Responses(1,2,3). *eNeuro* 3(1):ENEURO. 0067-0015.2015.

32. Bakkum DJ*, et al.* (2013) Parameters for burst detection. *Front Comput Neurosci* 7:193.

33. Turecek J, Han VZ, Cuzon Carlson VC, Grant KA, & Welsh JP (2016) Electrical Coupling and Synchronized Subthreshold Oscillations in the Inferior Olive of the Rhesus Macaque. *J Neurosci* 36(24):6497-6502.

34. Sugihara I, Lang EJ, & Llinas R (1993) Uniform olivocerebellar conduction time underlies Purkinje cell complex spike synchronicity in the rat cerebellum. *J Physiol* 470(1):243-271.

35. Davie JT, Clark BA, & Hausser M (2008) The origin of the complex spike in cerebellar Purkinje cells. *J Neurosci* 28(30):7599-7609.

36. Bengtsson F, Ekerot CF, & Jorntell H (2011) In vivo analysis of inhibitory synaptic inputs and rebounds in deep cerebellar nuclear neurons. *PLoS One* 6(4):e18822.

37. Tang T, Suh CY, Blenkinsop TA, & Lang EJ (2016) Synchrony is Key: Complex Spike Inhibition of the Deep Cerebellar Nuclei. *Cerebellum* 15(1):10-13.

38. Hoebeek FE, Khosrovani S, Witter L, & De Zeeuw CI (2008) Purkinje cell input to cerebellar nuclei in tottering: ultrastructure and physiology. *Cerebellum* 7(4):547-558.

39. Uno M, Yoshida M, & Hirota I (1970) The mode of cerebello-thalamic relay transmission investigated with intracellular recording from cells of the ventrolateral nucleus of cat's thalamus. *Exp Brain Res* 10(2):121-139.

40. Hua SE & Lenz FA (2005) Posture-related oscillations in human cerebellar thalamus in essential tremor are enabled by voluntary motor circuits. *J Neurophysiol* 93(1):117-127.

41. Ruigrok TJ & Voogd J (1995) Cerebellar influence on olivary excitability in the cat. *Eur J Neurosci* 7(4):679-693.

42. Devor A, Fritschy JM, & Yarom Y (2001) Spatial distribution and subunit composition of GABA(A) receptors in the inferior olivary nucleus. *J Neurophysiol* 85(4):1686-1696.

43. Pasquereau B, DeLong MR, & Turner RS (2016) Primary motor cortex of the parkinsonian monkey: altered encoding of active movement. *Brain* 139(Pt 1):127-143.

44. Isope P & Barbour B (2002) Properties of unitary granule cell-->Purkinje cell synapses in adult rat cerebellar slices. *J Neurosci* 22(22):9668-9678.

45. Mapelli J, Gandolfi D, & D'Angelo E (2010) High-Pass Filtering and Dynamic Gain Regulation Enhance Vertical Bursts Transmission along the Mossy Fiber Pathway of Cerebellum. *Front Cell Neurosci* 4:14.

46. Ito M, Yoshida M, Obata K, Kawai N, & Udo M (1970) Inhibitory control of intracerebellar nuclei by the purkinje cell axons. *Exp Brain Res* 10(1):64-80.

Neuron type	Parameter	Value	Source
ION	Length (μm)	20	Ref. (33)
	Diameter (μm)	20	Ref. (33)
	E_K (mV)	-70	Modified from ref. (3)
	E_{Na} (mV)	55	Ref. (3)
	g_{Kdr} (mS·cm^2)	9	Ref. (3)
	g_{Na} (mS·cm^2)	37	Ref. (3)
	g_h (mS·cm^2)	8e-2	Ref. (3)
	g_{Ca} (mS·cm^2)	0.27	Ref. (5)
	g_l (mS·cm^2)	0.13	Ref. (5)
	I_{OC} (nA)	$I_{OC} \sim \mathcal{U}$(-1.5,-1.15)×1e-3	Set to match the subthreshold oscillatory activity with ref. (7)
	σ_m (nA)	1e-5	
DCN	Length (μm)	65	Set to fit the *f-I* curve reported in ref. (8)
	Diameter (μm)	20.25	Ref. (8)
	E_K (mV)	-70	Modified from ref. (6)
	E_{Na} (mV)	61	Modified from ref. (6)
	g_{NaF} (mS·cm^2)	1.91e-2	Modified from ref. (6)
	I_{OC} (nA)	-5.3e-2	Set to adjust the baseline firing rate to values in refs. (13, 14)
	σ_m (nA)	5e-2	
NO	Length (μm)	200	Set to fit the *f-I* curve reported in ref. (8)
	Diameter (μm)	14.88	Ref. (8)
	g_{Kdr} (mS·cm^2)	2.86e-2	Modified from ref. (6)
	I_{OC} (nA)	-3e-2	Set to adjust the baseline firing rate to values in ref. (8)
	σ_m (nA)	2e-2	
PC	Q_{10}	2.2	Modified from ref. (9)
	I_{OC} (nA)	$I_{OC} \sim$-3e-4 + Γ(0.8,3.7e-3)	Set to adjust the baseline firing rate to values in ref. (9)
	σ_m (nA)	1e-6	
TC	Length (μm)	96	Ref. (12)
	Diameter (μm)	96	Ref. (12)
	σ_m (nA)	0.1	
PYN	I_{OC} (nA)	0.17	Modified from ref. (24)
	σ_m (nA)	0.1	
FSI	I_{OC} (nA)	0.15	Modified from ref. (24)
	σ_m (nA)	0.1	

Table S1. Parameters used in the proposed model. *Legend*: Γ(0.8,3.7e-3) is the gamma function with shape parameter k=0.8 and scale parameter θ=3.7e-3. $\mathcal{U}$(-1.5,-1.15) is the uniform distribution on the interval between the values -1.5 and -1.15.

Synapse	Parameter	Value	Source
ION→PC (AMPA)	$\tau^{ION\rightarrow PC\ (AMPA)}$ (ms)	0.6	Ref. (28)
	E_{syn} (mV)	0	Value used in every excitatory synapse
	Δt (ms)	4	Ref. (34)
	g_{syn} (uS)	4e-3	Set to reproduce the PC response in refs. (29, 35)
	σ_w	5e-9	Set to induce ±0.1 pA synaptic current fluctuation
ION→PC (NMDA)	$\tau_1^{ION\rightarrow PC\ (NMDA)}$ (ms)	2.63	Ref. (28)
	$\tau_2^{ION\rightarrow PC\ (NMDA)}$ (ms)	28	Ref. (28)
	E_{syn} (mV)	0	
	Δt (ms)	4	Ref. (34)
	g_{syn} (uS)	2.5e-3	Set to reproduce the PC response in refs. (29, 35)
	σ_w	5e-9	Set to induce ±0.1 pA synaptic current fluctuation
ION→PC (di-synaptic interneuron-mediated)	$\tau_1^{ION\rightarrow PC\ (LTD)}$ (ms)	5.0	Refs. (30, 31)
	$\tau_2^{ION\rightarrow PC\ (LTD)}$ (ms)	$\sim\mathcal{N}(\mu, \sigma^2)$, μ=80, σ=10	Refs. (30, 31)
	E_{syn} (mV)	-65	Refs. (30, 31)
	Δt (ms)	14	Ref. (34)
	g_{syn} (uS)	1e-2	Refs. (30, 31)
	σ_w	5e-9	Set to induce ±0.1 pA synaptic current fluctuation
ION→DCN	$\tau^{ION\rightarrow DCN}$ (ms)	0.8	Refs. (13, 21)
	E_{syn} (mV)	0	
	Δt (ms)	2.5	Ref. (13)
	g_{syn} (uS)	5e-3	Refs. (13, 20, 21)
	σ_w	1e-10	Set to induce ±2e-3 pA synaptic current fluctuation
PC→DCN	α	0.2	Set to reproduce the DCN response in refs. (20, 36)
	β	1	Set to reproduce the DCN response in refs. (20, 36)
	V_{off} (mV)	-52	Set to accommodate DCN response to PC CS
	$\tau^{PC\rightarrow DCN}$ (ms)	2.4	Refs. (8, 37)
	E_{syn} (mV)	-80	Ref. (6)
	Δt (ms)	4.2	Ref. (38)
	g_{syn} (uS)	1e-3	Set to reproduce the DCN response in refs. (20, 36)
	σ_w	1e-7	Set to induce ±5.5e-5 pA current fluctuation
PC→NO	α	0.2	Same as PC→DCN
	β	1	Same as PC→DCN
	V_{off} (mV)	-52	Same as PC→DCN
	$\tau^{PC\rightarrow NO}$ (ms)	35	Refs. (8, 38)
	E_{syn} (mV)	-80	Estimated from (8)
	Δt (ms)	4.2	Ref. (38)
	g_{syn} (uS)	2.8e-5	Set to adjust the *in vivo* firing rate in ref. (17)
	σ_w	1e-7	Set to induce ±2e-3 pA synaptic current fluctuation
DCN→TC	$\tau_1^{DCN\rightarrow Vim}$ (ms)	1.3	Ref. (39)
	$\tau_2^{DCN\rightarrow Vim}$ (ms)	20	Ref. (39)
	E_{syn} (mV)	0	
	Δt (ms)	2	Ref. (39)
	g_{syn} (uS)	1.5e-3	Set to reproduce the bursting behavior in ref. (40)
	σ_w	1e-5	Set to induce synaptic current fluctuation of ±0.2 nA
DCN→ION (dentato-rubro-	$\tau_1^{DCN\rightarrow ION}$ (ms)	2	Refs. (17, 41)
	$\tau_2^{DCN\rightarrow ION}$ (ms)	10	Refs. (17, 41)
	E_{syn} (mV)	0	
	Δt (ms)	15	Refs. (17, 41)

olivary pathway)	g_{syn} (uS)	8e-6	Refs. (17, 41)
	σ_w	1e-12	Set to induce ±2e-5 pA synaptic current fluctuation
NO→ION	$\tau_1^{NO\rightarrow ION}$ (ms)	40	Refs. (17, 27, 42)
	$\tau_2^{NO\rightarrow ION}$ (ms)	180	Refs. (17, 27, 42)
	E_{syn} (mV)	-65	Ref. (27)
	Δt (ms)	45	Refs. (17, 27)
	g_{syn} (uS)	3e-5	Refs. (17, 27)
	σ_w	1e-12	Set to induce ±2e-5 pA synaptic current fluctuation
PP→ION	$\tau_1^{PP\rightarrow ION}$ (ms)	2	Refs. (17, 41)
	$\tau_2^{PP\rightarrow ION}$ (ms)	10	Refs. (17, 41)
	E_{syn} (mV)	0	
	g_{syn} (uS)	1.5e-5	Set to adjust the *in vivo* firing rate as in ref. (1)
PYN→PYN	E_{syn} (mV)	0	Ref. (24)
	g_{syn} (uS)	2.7e-2×w, $w \sim \mathcal{N}(\mu, \sigma^2)$, μ=1, σ=0.2	Modified from ref. (24)
	σ_w	1e-5	Set to induce ±5.0 pA synaptic current fluctuation
FSI→FSI	E_{syn} (mV)	-80	Ref. (24)
	g_{syn} (uS)	1.5e-3	Modified from ref. (24)
	σ_w	1e-5	Set to induce ±0.3 pA synaptic current fluctuation
FSI→PYN	E_{syn} (mV)	-80	Ref. (24)
	g_{syn} (uS)	2.2e-2×w, $w \sim \mathcal{N}(\mu, \sigma^2)$, μ=1, σ=0.16	Modified from ref. (24)
	σ_w	1e-5	Set to induce ±4.0 pA synaptic current fluctuation
PYN→FSI	E_{syn} (mV)	0	Ref. (24)
	g_{syn} (uS)	2.5e-3	Modified from ref. (24)
	σ_w	1e-5	Set to induce ±0.5 pA synaptic current fluctuation
PP→PYN	$\tau^{PP\rightarrow PYN}$ (ms)	3	Modified from ref. (24)
	E_{syn} (mV)	0	Ref. (24)
	g_{syn} (uS)	2.2e-3×w, $w \sim \mathcal{N}(\mu, \sigma^2)$, μ=1, σ=0.5	Set to adjust the *in vivo* firing rate as in ref. (43)
TC→PYN	$\tau^{Vim\rightarrow PYN}$ (ms)	5.26	Ref. (24)
	E_{syn} (mV)	0	Ref. (24)
	Δt (ms)	1	
	g_{syn} (uS)	1.5e-2×w, $w \sim \mathcal{N}(\mu, \sigma^2)$, μ=1, σ=0.25	Refs. (24, 43)
	σ_w	1e-6	Set to induce ±0.2 nA synaptic current fluctuation
PYN→TC	$\tau^{PYN\rightarrow Vim}$ (ms)	5.26	Ref. (24)
	E_{syn} (mV)	0	Ref. (24)
	Δt (ms)	1	
	g_{syn} (uS)	9e-4×w, $w_\in$ [0.64,1.36,0.60,1.53]	Modified from ref. (24)
	σ_w	1e-6	Set to induce ±0.2 nA synaptic current fluctuation
TC→FSI	$\tau^{Vim\rightarrow FSI}$ (ms)	5.26	Ref. (24)
	E_{syn} (mV)	0	Ref. (24)
	Δt (ms)	2	
	g_{syn} (uS)	9e-4	Modified from ref. (24)
	σ_w	1e-6	Set to induce ±0.2 nA synaptic current fluctuation
PYN→GrC (AMPA)	E_{syn} (mV)	0	Ref. (10)
	Δt (ms)	4	Ref. (10, 15)

	g_{syn} (nS)	3.48	Modified from ref. (10)
PYN→GrC (NMDA)	E_{syn} (mV)	0	Ref. (10)
	Δt (ms)	4	Ref. (10, 15)
	g_{syn} (nS)	0.348	Modified from ref. (10)
PYN→GoC	E_{syn} (mV)	0	Ref. (10)
	Δt (ms)	4	Ref. (10, 15)
	g_{syn} (nS)	50	Modified from ref. (10)
GrC→GoC	E_{syn} (mV)	0	Ref. (10)
	Δt (ms)	1	Ref. (10)
	g_{syn} (nS)	300	Modified from ref. (10)
GrC→STC	E_{syn} (mV)	0	Ref. (10)
	Δt (ms)	1	Ref. (10)
	g_{syn} (nS)	30	Modified from ref. (10)
GoC→GrC	E_{syn} (mV)	-65	Ref. (10)
	Δt (ms)	0.5	Ref. (10)
	g_{syn} (nS)	6	Modified from ref. (10)
STC→GoC	E_{syn} (mV)	-65	Ref. (10)
	Δt (ms)	1	Ref. (10)
	g_{syn} (nS)	12.5	Modified from ref. (10)
GrC→PC	$\tau_1^{GrC\rightarrow PC}$ (ms)	1.2	Ref. (10, 44)
	$\tau_2^{GrC\rightarrow PC}$ (ms)	14	Ref. (10, 44)
	E_{syn} (mV)	0	
	Δt (ms)	$\Delta t \sim \mathcal{U}(0, 10)$	Estimated from (45)
	g_{syn} (uS)	3.27e-5×w, $w \sim \mathcal{N}(\mu, \sigma^2)$, μ=1, σ=0.5	Set to match the *in vivo* firing rate as in ref. (2)
	σ_w	5e-9	Set to induce ±0.1 pA synaptic current fluctuation
PYN→DCN (AMPA)	$\tau^{PYN\rightarrow DCN\ (AMPA)}$ (ms)	1	Ref. (16)
	E_{syn} (mV)	0	
	Δt (ms)	1.7	Ref. (16)
	g_{syn} (uS)	2.1e-4	Relative amplitude vs NMDA: ref. (16); set to match *in vivo* firing rate in ref. (2)
	σ_w	1e-10	Set to induce ±5.5e-5 pA current fluctuation
PYN→DCN (NMDA)	$\tau_1^{PYN\rightarrow DCN\ (NMDA)}$ (ms)	1	Ref. (16)
	$\tau_2^{PYN\rightarrow DCN\ (NMDA)}$ (ms)	6	Ref. (16)
	E_{syn} (mV)	0	
	Δt (ms)	1.7	Ref. (46)
	g_{syn} (uS)	1.26e-4	Set to match *in vivo* firing rate in ref. (2)
	σ_w	1e-10	Set to induce ±5.5e-5 pA current fluctuation

Table S2. Synaptic mechanisms used in the model. *Legend*: CS = complex spike; GrC = granule cell; GoC = Golgi cell; STC = stellate cell. PP = presynaptic Poisson process source input to ION or PYN neurons. w $\sim\mathcal{N}(\mu, \sigma^2)$, is the Gaussian distribution with mean μ and standard deviation σ.